THE JOURNAL OF PHYSICAL CHEMISTRY A
A JOURNAL OF THE AMERICAN CHEMICAL SOCIETY

pubs.acs.org/JPCA

Article

Imaging the Photodissociation Dynamics and Fragment Alignment of CH_2BrI at 193 nm

Published as part of The Journal of Physical Chemistry virtual special issue "Paul L. Houston Festschrift".

Pedro Recio, Javier Cachón, Luis Rubio-Lago, David V. Chicharro, Alexandre Zanchet, Paulo Limão-Vieira, Nelson de Oliveira, Peter C. Samartzis, Sonia Marggi Poullain, and Luis Bañares*

Cite This: *J. Phys. Chem. A* 2022, 126, 8404–8422

Read Online

ACCESS | Metrics & More | Article Recommendations | Supporting Information

ABSTRACT: The photodissociation dynamics and photofragment alignment of bromoiodomethane (CH_2BrI) have been studied at 193 nm using a double experimental and theoretical approach. In addition, the ultraviolet (UV)-vacuum ultraviolet (VUV) absorption spectrum of gas phase CH_2BrI has been measured in the photon energy range of 5−11 eV using the VUV Fourier transform spectrometer (FTS) at the VUV beamline DESIRS of the synchrotron SOLEIL facility. The slice imaging technique in combination with resonance enhanced multiphoton ionization (REMPI) detection of the $Br(^2P_J)$ and $I(^2P_J)$ (with J = 3/2 and 1/2 for Br/I and Br*/I*, respectively) atomic photofragments have been used to produce experimental translational energy and angular distributions, which were analyzed to deliver, on one hand, the partitioning of the available energy among the different degrees-of-freedom of the photofragments and, on the other, the photofragment polarization in terms of $a_q^k(p)$ alignment parameters. The experimental measurements were rationalized in terms of high-level *ab initio* calculations of vertical excitation energies, transition dipole moments and potential energy curves (PECs) along different reaction coordinates to provide a complete picture of the photodissociation dynamics. The results indicate that for excitation at 193 nm, prompt C−X cleavage (with X being either halogen atom, Br or I) competes with fast internal conversion and consequent stochastic dissociation in lower electronic states. In the case of the $CH_2Br + I(^2P_{3/2})/I^*(^2P_{1/2})$ channels, the dynamics are greatly biased toward the stochastic dissociation process due to both the particular PECs landscape and the unfavored excitation of the CH_2BrI ensemble with respect to the C−I molecular axis at this excitation energy. The *ab initio* PECs provide a tentative path for the fast dissociation process in either case. For the C−Br bond breakage, excitation to the 13A' electronic state and predissociation through the 11A'/11A'' or 12A'/12A'' states, leading to direct dissociation through the 10A'/9A'' states, appear as the most consistent dynamics. For the C−I channel, predissociation does not become a reliable possibility and a fast internal conversion may precede dissociation through the repulsive 6A'/6A'' and 4A'/4A'' states. The large content of rotational and vibrational excitation of the polyatomic cofragments is justified through the soft impulsive model and the geometrical changes produced along the dissociation pathway. Strikingly, the $a_q^k(p)$ alignment parameters obtained for the $Br(^2P_{3/2})$ and $I(^2P_{3/2})$ photoproducts indicate that the rotational angular momentum of the CH_2X (X = I or Br) cofragment appears highly constrained along the recoil direction. Finally, this work presents a highly plausible explanation for the branching ratio of secondary dissociation processes in the photodynamics of CH_2BrI at 193 nm.

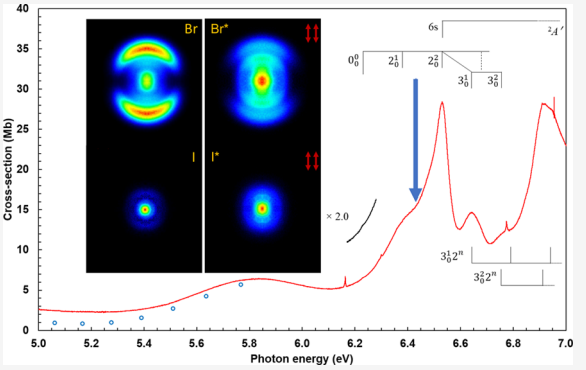

INTRODUCTION

Halocarbons (R−X, where R is an alkyl radical and X = Cl, Br, I) have revived significant attention in several chemistry areas due to their role in the troposphere chemistry. In particular, photolysis of halocarbons yields atomic halogen fragments, able to react with other particles of the atmosphere and produce pollutant species.[1,2] In addition, reactive halogen atoms have an important effect on ozone depletion, which constitutes one of the biggest atmospheric problems of the last century.[3−5] Dihalocarbons, as bromoiodomethane (CH_2BrI), become even more relevant due to the presence of two halogen atoms. Another characteristic of dihalocarbons that increases their interest is the intricate structure of the excited states involved in

Received: August 17, 2022
Revised: October 13, 2022
Published: November 2, 2022

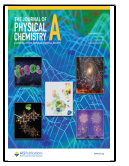

their photochemistry. As such, they are amenable to be used as prototypes for bond-selective electronic excitation and dissociation.

The UV absorption spectrum of CH_2BrI is well-known to consist of three bands.[6] The first absorption band (A band), centered at 268 nm, has been attributed almost exclusively to the $\sigma^*(C-I) \leftarrow n(I)$ transition and C−I bond dissociation. In contrast, the second absorption band (that will be named here as A' band) is centered at 210 nm and has been assigned to the $\sigma^*(C-Br) \leftarrow n(Br)$ transition and C−Br bond breakage. The third band,[7,8] which starts around 200 nm, has been assigned to a Rydberg transition on the I atom.

Lee and Bersohn[9] published, in 1982, an investigation on the photodissociation of CH_2BrI at 258 nm using photofragment translational spectroscopy. A more detailed investigation using the same technique was published later by Butler et al.,[8] who measured the photodissociation from the three absorption bands by exciting the molecule at 248, 210, and 193 nm, and validated the bond selectivity photochemistry typical of dihalocarbons. In the A band (at 248 nm), dissociation of the C−I bond was confirmed to be the major decomposition process although a small contribution of C−Br bond fission was confirmed. In the A' band (at 210 nm), cleavage of C−Br bond was the only decomposition pathway observed for the title molecule. At higher excitation energies (at 193 nm), besides the C−Br and C−I bond fissions—with dominance of the former over the latter—the presence of a third dissociation channel was detected, specifically, IBr formation produced by concerted elimination. At such high excitation energies, both halogen atoms were mainly produced in the spin−orbit excited state, $^2P_{1/2}$, while the IBr fragment was concluded to be formed exclusively in high electronic excited states.[8] The photofragment polarization analysis performed in the same work was consistent with a mechanism where the excitation is produced to a Rydberg level of the iodine atom and consequent predissociation on a longer time scale than the rotational period of the parent molecule. The bond selectivity proposed by Butler et al.[8] was confirmed later on by the theoretical calculations of Liu et al.[10] and Lindh and co-workers,[11] who calculated the vertical excitation energies and oscillator strengths for the excited states comprising the A and A' bands and the potential energy curves (PECs), respectively, for both C−Br and C−I bond fission dissociation channels. Lindh and co-workers[11] also studied the isomerization process to *iso*-CH_2−Br−I and *iso*-CH_2−I−Br. Isomerization processes have been largely reported in experimental studies of CH_2BrI in solution.[7,12,13] Using different solvents and matrices, it was demonstrated the solvent-induced character of the isomerization process as well as the observed coupling between the $\sigma^*(C-I) \leftarrow n(I)$ and the $\sigma^*(C-Br) \leftarrow n(Br)$ transitions at specific wavelengths.

Further experimental studies on the photodissociation of CH_2BrI that delve into the electronic structure of the molecule have been carried out by different groups. Leone and co-workers,[14] for instance, performed experiments using femtosecond time-resolved extreme ultraviolet (XUV) transient absorption spectroscopy, following excitation at 266 nm. Similar results as those published by Butler et al.[8] were reported. In particular, dissociation in the A band was dominated by C−I dissociation (about 80%), and C−Br dissociation was observed as a minor pathway. The technique employed allows the transient characterization of the dissociation process and thus, a slow dissociation dynamics of the C−Br bond cleavage was determined, which was rationalized in terms of the difference between the repulsive slopes of the excited states and the relative internal energy deposited into the CH_2I radical.

Weinacht and co-workers,[15,16] using ultraviolet (UV)-pump, vacuum ultraviolet (VUV)-probe time-resolved photoelectron spectroscopy, velocity map imaging (VMI), and *ab initio* calculations, compared the photodissociation of CH_2I_2 and CH_2BrI at 267 nm. The photodissociation of CH_2BrI was described as a direct decomposition process along the C−I coordinate. However, C−I bond dissociation of CH_2I_2 should involve internal conversion and motion along multiple dimensions. These conflicts in the photodissociation mechanisms arise from differences in the nonadiabatic couplings between electronic states of the two molecules. Coulomb explosion imaging has been employed by Burt et al.[17] in a UV pump−IR probe scheme to observe the dissociation dynamics following excitation at 271.6 nm. The results, consistent with previous results from Butler and co-workers,[8] revealed in particular secondary dissociation of CH_2Br through a second UV-photon absorption. Köckert and co-workers[18] have recently published a work where UV pump−XUV probe pulses along with multimass ion imaging were used to study the photodissociation of CH_2BrI at 271 nm in the A band yielding the CH_2Br + I channel, where the influence of parent rotation on a charge transfer process was investigated. The results suggest that, in spite of the slow dissociation, the critical interatomic distance for charge transfer is rapidly reached.

Pan et al.[19] published a VMI study on the photodissociation of CH_2BrI centered on the first absorption A-band (280−310 nm) in which both spin−orbit $I(^2P_{3/2})$ and $I^*(^2P_{1/2})$ photofragments were detected by (2 + 1) resonance-enhanced multiphoton ionization (REMPI). The results concluded that most of the available energy was partitioned into internal energy of the CH_2Br radical, while only a small amount was imparted to the photofragments. The reported behavior was consistent with a simple impulsive model in agreement with Butler et al.[8] Finally, Lin and co-workers[20] studied the photodissociation of CH_2BrI at 243 nm by using cavity ring-down spectroscopy seeking for elimination of IBr. The ground state IBr fragment was observed and characterized by a vibrational population of 1:0.58:0.34 for the vibrational $v'' = 0, 1, 2$ levels, respectively. The quantum yield of this channel was determined as well, and the considerably low value of 0.044 found was consistent with what Butler et al.[8] predicted in the A' band (at 210 nm).

The aim of the present study is to investigate the photodissociation dynamics and the atomic photofragment alignment of CH_2BrI in the B-band excited at 193 nm through the detection of iodine, $I(^2P_{3/2})$ and $I^*(^2P_{1/2})$, and bromine, $Br(^2P_{3/2})$ and $Br^*(^2P_{1/2})$, photofragments by using pump−probe nanosecond lasers and the slice imaging technique coupled to (2 + 1) REMPI detection, in combination with *ab initio* electronic structure calculations of vertical excitation energies, transition dipole moments and potential energy curves up to 10 eV. In addition, we have measured the gas phase high-resolution UV−VUV absorption spectrum in order to assign the different electronic states accessed by UV−VUV one-photon excitation in this region. The present study is as an extension of a previous publication,[21] where the photodissociation of bromoiodomethane was investigated around the maximum of the first two absorption bands, the A and A' bands, at 266 and 210 nm, respectively. In a similar fashion than that of the present work, the formation of the $I(^2P_{3/2})$, $I^*(^2P_{1/2})$, $Br(^2P_{3/2})$, and $Br^*(^2P_{1/2})$ photoproducts was experimentally characterized by using the VMI and slice imaging (SI) techniques and

https://doi.org/10.1021/acs.jpca.2c05897
J. Phys. Chem. A 2022, 126, 8404−8422

rationalized with the aid of high level *ab initio* calculations. It was concluded in the said work that the I atoms were produced from the A band through direct dissociation in the $5A'$ excited state, while the formation of I* atoms involved the $5A' \rightarrow 4A'/4A''$ nonadiabatic crossing. Furthermore, the presence of a minor contribution of Br and Br* atoms in the photodissociation from the A band was attributed to indirect dissociation via a curve crossing between the $5A'$ state and an upper excited state. Dissociation in the A' band was characterized, in contrast, by a strong photoselectivity, since no I or I* atoms were observed. The dissociation leading to Br and Br* atoms was proposed to occur via the $9A'$, $8A''$, and $10A''$ excited states. In 2018, a complementary femtosecond time-resolved VMI experiment of bromoiodomethane and chloroiodomethane was published by some of the authors of the present work.[22] CH_2BrI was excited at 268 nm in the first A absorption band and the I/I* fragments were detected by (2 + 1) REMPI. Asymptotic images were measured, and the transients obtained permitted the determination of reaction times. In addition, high level *ab initio* electronic structure calculations and full dimension on-the-fly trajectory calculations including surface hopping were performed, yielding CH_2Br and I/I* products. The main finding of this work was an *anchor* effect due to the substituent Br atom in the parent molecule, which implies significant rotational motion of the dissociating molecule, and leads to a remarkable rotational energy of the CH_2Br radical cofragment. It was concluded that this energy flux into internal degrees of freedom of the molecule is the main key factor governing the real time photodissociation dynamics,[22] which was very much in agreement with the conclusions found by Köckert et al.[18]

The region of the VUV absorption spectrum of CH_2BrI in which the present work focuses has not received as much attention as the A and A' bands. As introduced in the previous paragraphs, only Butler et al.[8] studied thoroughly the photodissociation of the title molecule at 193 nm using photofragment translational spectroscopy. Hence, a deep investigation of the photodissociation dynamics of CH_2BrI at this excitation wavelength (193 nm) seemed very timely considering the complex excitation to a region congested with many excited states of Rydberg character and the complex dissociation mechanisms expected. We have included measurements of the stereodynamics of the photodissociation process by determining the atomic photofragment alignment parameters to give light into de different possible mechanisms at play. The support of high level *ab initio* electronic structure calculations including vertical excitation energies, transition dipole moments and potential energy curves for different internal coordinates is crucial to interpret the experimental results in an excitation region where different dissociation mechanisms compete.

The present work is divided in the following sections. The experimental and theoretical approaches are explained in the Methods section, as well as, the methodology employed to determine the stereodynamics of the process in the form of atomic photofragment alignment. In the Experimental Results and Theoretical Results sections the most relevant experimental and theoretical results are presented, respectively. In the Analysis and Discussion section both experimental and theoretical results are discussed jointly. Finally, the main conclusions of this work are presented in the Conclusions section.

METHODS

Experimental Setups. The high-resolution UV−VUV absorption spectrum of gas phase CH_2BrI was measured using the VUV Fourier transform spectrometer (FTS),[23] which is one of the permanent endstations of the VUV beamline DESIRS[24] at the synchrotron SOLEIL facility. The VUV FTS covers a large UV−VUV spectral range from 4 to 30 eV with a line width of 0.08 cm^{-1} on a large spectral window ($\Delta E/E$ = 7%),[25] over which all spectral features can be acquired in a multiplex way. The detailed description of the beamline and the VUV FTS instrument can be found in refs.[25,26] In brief, the FTS measurement implies a two steps procedure. A first absorption measurement covering the full VUV spectral range is completed using a windowless cell. A reservoir filled with the liquid sample is connected to the main sample environmental vacuum chamber. After a series of freeze, pump, and thaw purification steps of the sample, the sample in the gas phase controlled by a needle valve is allowed to flow through a 10 cm cylindrical windowless cell with two rectangular tubes at both ends. The synchrotron beam is going through the cell and is ultimately recorded by the FTS instrument. In order to calibrate the column density, another measurement at moderate spectral resolution is performed inside a 9 cm long MgF_2 windowed cell. This time, only a few spectral windows are recorded, providing absolute absorption cross sections. The windowless spectrum is scaled upon these reference points following the procedure detailed in ref 25. The VUV-FTS is extremely sensitive to external perturbation,[25] a statistical study gave an estimated uncertainty for the absolute cross-section of ±10%. Concerning the energy scale, no further calibration is required for this experiment since the accuracy is intrinsically referred to the indexation HeNe stabilized laser leading already to a relative error in the range of 10^{-6}.[23] The spectral resolution was set to 4.3 cm^{-1}, which is more than sufficient to depict the quite broad structures of CH_2BrI. Due to the high flux, we have noticed signatures of photolysis products of CH_2BrI in the spectrum, those are in general quite weak. Most of these signatures have been identified and are listed in Table S1 of the Supporting Information (SI).

The nanosecond laser pump−probe and slice imaging experimental setup at FORTH-IESL used in the present experiments has been already described in detail elsewhere[27−30] and only a brief description is presented here. A molecular beam is created by expanding a gas mixture of CH_2BrI in He (10%, 1 atm backing pressure) into vacuum using a piezoelectric pulsed valve working at a repetition rate of 10 Hz. The beam passes through a skimmer and is collimated to a diameter of 1 mm prior to intersect focused laser beams at right angles. Excitation of CH_2BrI was carried out at 193 nm using an excimer laser (Lambda Physik COMPEX, operating with ArF), linearly polarized using Brewster reflection. For the detection of the fragments a MOPO (Spectra-Physics 730D10) pumped by a Nd:YAG laser (Quanta Ray Pro 250) and delayed 10 ns with respect to the pump laser was used. (2 + 1) REMPI detection of $Br(^2P_{3/2})$ and $Br^*(^2P_{1/2})$ was carried out at 250.35 and 262.45 nm, respectively, through the transitions $(^3P)5p(^2S_{1/2}) \leftarrow 5p(^2P_{3/2})$ and $(^3P)5p(^2S_{1/2}) \leftarrow 5p(^2P_{1/2})$.[31] The $I(^2P_{3/2})$ and $I^*(^2P_{1/2})$ products were detected at 304.58 and 305.49 nm, respectively, for the $(^3P_2)6p[3]_{7/2} \leftarrow 5p(^2P_{3/2})$ and $(^3P_1)$-$6p[1]_{3/2} \leftarrow 5p(^2P_{1/2})$ transitions.[32] The generated Br^+ and I^+ ions are projected onto the position-sensitive detector system (two microchannel plates MCPs coupled to a phosphor screen).

https://doi.org/10.1021/acs.jpca.2c05897
J. Phys. Chem. A 2022, 126, 8404−8422

Slice images of Br^+ or I^+ are recorded using a 500 ns pulsed extraction delay applied on the repeller plate and an effective 10 ns detector gate on the front MCP. As Br presents two isotopes ^{79}Br and ^{81}Br with similar abundance, it is necessary to select an extraction delay allowing a complete separation of the ion clouds from both isotopes such that the imaged slice correspond to a single isotope, $^{79}Br^+$ in the present case. The images for $Br(^2P_{3/2})$ and $I(^2P_{3/2})$, where atomic alignment effects can be expected, were recorded using the three laser polarization configurations: X(pump)X(probe), XZ, and ZX, where X is perpendicular to the laser propagation axis and Z is parallel to the molecular beam. However, the images for the $Br^*(^2P_{1/2})$ and $I^*(^2P_{1/2})$ fragments were recorded only for both lasers parallel to the detector (XX) since these fragments cannot present any alignment effects.[a] The ZZ images, which do not contain any dynamical information, were obtained in all cases as a reference to avoid systematic errors, such as detector inhomogeneities.

The sliced images were quadrant symmetrized prior to extracting the kinetic energy and angular distributions. For all the two-color pump−probe measured images, the contribution of each laser alone was subtracted, so that the observed signal was only pump−probe.

Atomic Alignment Analysis. The slice imaging technique provides a direct measurement of the central slice of the 3D photofragment distribution produced in a photodissociation process. Such development constitutes one of the main advantages of the technique, since it that does not demand for any mathematical transformation to map the photofragment distribution. The slice images can be, therefore, straightforwardly interpreted to extract the relevant dynamical information.

The analysis process requires slice images acquired in four combinations of the pump and probe laser polarizations, namely, X(pump)X(probe), XZ, ZX, and ZZ configurations. The XYZ axis system denotes the laboratory frame, with both lasers counterpropagating along the Y axis, and the molecular beam propagating along the Z axis (the time-of-flight axis). In such fashion, the XX images comprise all the stereodynamical information, *i.e.*, the anisotropy of the dissociation process and the orientation and/or alignment of the photoproducts. For the XZ images, the probe polarization vector lies perpendicular to the detection plane and, therefore, all the information related to the angular momenta of the products is lost. Similarly, the ZX images have lost the information related to the anisotropy of the dissociation process. The ZZ images do not contain any dynamical information and are used as a reference to avoid systematic errors.

Among the relevant information that can be extracted from the images, photofragment alignment plays a key role to understand the underlying dynamics. The laboratory intensity distribution of a one-photon dissociation process and $(n + m)$ REMPI detection is given by the expression[33]

$$I(\theta_{pump}) \times I(\theta_{probe}) = [1 + \beta P_2(\cos\theta_{pump})] \times \sum_{k=2}^{2n+m} 1 + A_0^k P_k(\cos\theta_{probe}) \quad (1)$$

where $I(\theta_{pump})$ and $I(\theta_{probe})$ are the intensity distributions associated with the photolysis and detection processes, respectively, with θ_{pump} and θ_{probe} denoting the angle between the photolysis and probe polarization directions with respect to the recoil direction; β is the dissociation anisotropy parameter, A_0^k are the photofragment polarization parameters and $P_k(\cos\theta)$, the k-th Legendre polynomial.

When using linearly polarized pump and probe laser pulses, the experiment is not sensitive to photofragment orientation and the k index takes only even values. In addition, for $(2 + 1)$ REMPI detection, as used in this work, the expansion is truncated at $k = 4$ and eq 1 should be expressed as an expansion of Legendre polynomials up to $k = 6$[34,35]

$$I(\theta)^{FG} = 1 + \beta_2^{FG} P_2(\cos\theta) + \beta_4^{FG} P_4(\cos\theta) + \beta_6^{FG} P_6(\cos\theta) \quad (2)$$

where F and G denote the photolysis and probe polarization directions, respectively, with respect to the slicing plane XY (perpendicular to the time-of-flight axis Z), and β_k^{FG} are the anisotropy parameters in the laboratory frame. The phenomenological β_k^{FG} parameters comprise all the dynamical and geometrical information on the process. In order to extract the dynamical data, the β_k^{FG} must be transformed into a different set of parameters.

Rakitzis and Zare described the stereodynamics of molecular photodissociation in terms of a set of polarization parameters, the $a_q^k(p)$.[33] In a series of subsequent publications, Rakitzis established useful expressions for different laboratory geometries and dynamical problems;[34] among those, he established the relationship between the laboratory frame anisotropy parameters, β_k, and the molecular frame polarization parameters, $a_q^k(p)$, through the following expressions in terms of $A_q^k(p)$ coefficients

$$\beta_2 N = c\beta + s_2\left\{A_0{}^2(\text{iso}) + \frac{1}{7}[2A_0{}^2(\text{aniso}) + cA_1{}^2 - 2cA_2{}^2]\right\} + s_4\left\{\frac{1}{21}[6A_0{}^4(\text{aniso}) + \sqrt{30}\,cA_1{}^4 + \sqrt{15}\,cA_2{}^4]\right\} \quad (3a)$$

$$\beta_4 N = s_2\left\{\frac{1}{35}[18A_0{}^2(\text{aniso}) - 12cA_1{}^2 + 3cA_2{}^2]\right\} + s_4\left\{A_0{}^4(\text{iso}) + \frac{1}{77}[20A_0{}^4(\text{aniso}) + \sqrt{30}\,cA_1{}^4 + 6\sqrt{15}\,cA_2{}^4]\right\} \quad (3b)$$

$$\beta_6 N = s_4\left\{\frac{1}{35}[15A_0{}^4(\text{aniso}) - 2\sqrt{30}\,cA_1{}^4 + \sqrt{15}\,cA_2{}^4]\right\} \quad (3c)$$

where N, proportional to the population, is given by

$$N = 1 + s_2\left\{\frac{1}{5}[A_0{}^2(\text{aniso}) + cA_1{}^2 + cA_2{}^2]\right\} \quad (3d)$$

The s_k are the kth-order sensitivity factors (normalized so that $s_0 = 1$), and c is a constant that can take the values 1 or −1/2 for linear or circular polarization of the photolysis laser, respectively; for the work presented here $c = 1$, since only linear polarization of the photolysis laser has been employed. The

https://doi.org/10.1021/acs.jpca.2c05897
J. Phys. Chem. A 2022, 126, 8404−8422

Table 1. Theoretical Vertical Excitation Energies (VEE) at the Franck−Condon (FC) Geometry, Symmetry in C_s, and Transition Dipole Moments (TDM) for Each Axis *X*, *Y*, and *Z*, of the First 36 Spin-Orbit States[a]

state number	VEE (eV)	symmetry	TDM (Debye)	*X*	*Y*	*Z*
1	0	1*A*′	1.30986	0.00000	1.30410	0.12275
2	4.133	1*A*″	0.00613	0.00613	0.00000	0.00000
3	4.133	2*A*′	0.00600	0.00000	0.00108	0.00590
4	4.256	2*A*″	0.11184	0.11184	0.00000	0.00000
5	4.319	3*A*′	0.22751	0.00000	0.07456	0.21495
6	4.584	3*A*″	0.00457	0.00457	0.00000	0.00000
7	4.705	4*A*′	0.12771	0.00000	0.00440	0.12763
8	4.932	5*A*′	0.59943	0.00000	0.17768	0.57249
9	4.948	4*A*″	0.30256	0.30256	0.00000	0.00000
10	5.322	5*A*″	0.01374	0.01374	0.00000	0.00000
11	5.370	6*A*′	0.29829	0.00000	0.07993	0.28738
12	5.408	6*A*″	0.15374	0.15374	0.00000	0.00000
13	5.568	7*A*′	0.21505	0.00000	0.00908	0.21486
14	5.626	7*A*″	0.02479	0.02479	0.00000	0.00000
15	5.641	8*A*′	0.06915	0.00000	0.04068	0.05592
16	6.088	8*A*″	0.09765	0.09765	0.00000	0.00000
17	6.123	9*A*′	1.12145	0.00000	0.01733	1.12132
18	6.362	9*A*″	0.00291	0.00291	0.00000	0.00000
19	6.371	10*A*″	0.02094	0.02094	0.00000	0.00000
20	6.386	10*A*′	0.13551	0.00000	0.00859	0.13524
21	6.964	11*A*′	0.24789	0.00000	0.09803	0.22768
22	6.990	11*A*″	0.00676	0.00676	0.00000	0.00000
23	6.997	12*A*″	0.03406	0.03406	0.00000	0.00000
24	7.010	12*A*′	0.08612	0.00000	0.06370	0.05795
25	7.322	13*A*′	0.66826	0.00000	0.06924	0.66467
26	7.412	13*A*″	0.00253	0.00253	0.00000	0.00000
27	7.425	14*A*′	0.05863	0.00000	0.02062	0.05489
28	7.525	14*A*″	0.03169	0.03169	0.00000	0.00000
29	7.571	15*A*′	0.24548	0.00000	0.03467	0.24302
30	7.578	15*A*″	0.00353	0.00353	0.00000	0.00000
31	7.619	16*A*′	0.28788	0.00000	0.06907	0.27947
32	7.697	16*A*″	0.10122	0.10122	0.00000	0.00000
33	8.041	17*A*′	1.41181	0.00000	0.10479	1.40792
34	8.132	17*A*″	0.00279	0.00279	0.00000	0.00000
35	8.139	18*A*″	0.01123	0.01123	0.00000	0.00000
36	8.157	18*A*′	0.75683	0.00000	0.04372	0.75557

[a]The *X* axis is located perpendicular to the Br−C−I plane, while the *Y* and *Z* axis are in the plane, *Y* being perpendicular to C−Br and pointing roughly between Br and I, and *Z* being parallel to Br−I.

$A_q^k(p)$ coefficients in eqs 3a−3d) are related to the $a_q^k(p)$ parameters and are used to simplify the equations.[b]

Equations 3a−3d constitute the major result of Rakitzis' work[34] (presented as eqs 7a−7d in ref 34) since they lead to various sets of easy-to-handle expressions to analyze the experimental data.[34,36,37]

The $a_q^k(p)$ parameters can be classified into three different groups, i.e., $a_q^k(\|)$, $a_q^k(\perp)$, and $a_q^k(\|, \perp)$, according to the transition dipole moment of the one-photon excitation process. For a one-photon pure parallel transition (described by $\beta = 2$), $q = 0$, and we shall have only the $a_0^k(\|)$ parameters. For a one-photon pure perpendicular transition (described by $\beta = -1$), $q = 0, 2$, and the polarization is described by $a_q^k(\perp)$ parameters. The $a_q^k(\|, \perp)$ parameters represent contributions that arise from the interference between parallel and perpendicular transitions. Equations 3a−3d have been transformed by Rakitzis into straightforwardly implementable expressions for pure perpendicular transitions and even for the complicated interference case. To the best of our knowledge, such set of expressions have not been explicitly unraveled for a pure parallel transition, although the $a_q^k(p)$ formalism has been indeed used in several works.[36,37] In the following paragraphs, this gap is straightened out and the equivalent set of equations for parallel transitions (with and without the possibility of interferences from perpendicular transitions) are developed.

For a parallel transition, the $A_q^k(p)$ coefficients are expressed as

$$\begin{aligned} A_0^k(\text{iso}) &= a_0^k(\|) \\ A_0^k(\text{aniso}) &= 2a_0^k(\|) \\ A_1^k &= \sqrt{\frac{8}{3}}\, Re[a_1^k(\|, \perp)] \\ A_2^k &= 0 \end{aligned} \tag{4}$$

https://doi.org/10.1021/acs.jpca.2c05897
J. Phys. Chem. A 2022, 126, 8404−8422

Substitution of eq 4 into eqs 3a−3d results in the following equations

$$\beta_2 N = \beta + s_2\left\{\frac{11}{7}{a_0}^2(\|) + \frac{1}{7}\sqrt{\frac{8}{3}}Re[{a_1}^2(\|,\perp)]\right\} + s_4\left\{\frac{12}{21}{a_0}^4(\|) + 4\sqrt{5}Re[{a_1}^2(\|,\perp)]\right\} \quad (5a)$$

$$\beta_4 N = s_2\left\{\frac{36}{35}{a_0}^2(\|) - 12\sqrt{\frac{8}{3}}Re[{a_1}^2(\|,\perp)]\right\} + s_4\left\{\frac{117}{77}{a_0}^4(\|) + \frac{4}{77}\sqrt{5}Re[{a_1}^4(\|,\perp)]\right\} \quad (5b)$$

$$\beta_6 N = s_4\left\{\frac{10}{11}{a_0}^4(\|) - \frac{8}{33}\sqrt{\frac{8}{3}}Re[{a_1}^4(\|,\perp)]\right\} \quad (5c)$$

$$N = 1 + s_2\left\{\frac{1}{5}\left[2{a_0}^2(\|) + \sqrt{\frac{8}{3}}Re[{a_1}^2(\|,\perp)]\right]\right\} \quad (5d)$$

For experimental results that can be fitted to eq 2 with $\beta_6 = 0$ (as those acquired in the present work), the second order sensitivity parameter, s_4 is equal to 0; the relationship between the measured β_k^{FG} and the alignment parameters β, $a_0^k(\|)$, and $Re[a_1^k(\|,\perp)]$, for the three *FG* geometries, *XX*, *XZ*, and *ZX*, are given, therefore, by

$$\beta_2^{XX} = \frac{\beta + \frac{s_2}{7}\left\{11{a_0}^2(\|) + \sqrt{\frac{8}{3}}Re[{a_1}^2(\|,\perp)]\right\}}{1 + \frac{s_2}{5}\left\{2{a_0}^2(\|) + \sqrt{\frac{8}{3}}Re[{a_1}^2(\|,\perp)]\right\}} \quad (6a)$$

$$\beta_4^{XX} = \frac{12s_2\left\{\frac{3}{35}{a_0}^2(\|) + \sqrt{\frac{8}{3}}Re[{a_1}^2(\|,\perp)]\right\}}{1 + \frac{s_2}{5}\left\{2{a_0}^2(\|) + \sqrt{\frac{8}{3}}Re[{a_1}^2(\|,\perp)]\right\}} \quad (6b)$$

$$\beta_2^{XZ} = \frac{\beta + s_2{a_0}^2(\|)}{1 + \frac{1}{2}s_2{a_0}^2(\|)} \quad (6c)$$

$$\beta_2^{ZX} = s_2{a_0}^2(\|) \quad (6d)$$

The s_2 coefficient is calculated according to Table 1 in ref 34 (including the long-time-limit hyperfine depolarization coefficient[38] of 10/37) yielding values of −25/74 and 80/333 for $Br(^2P_{3/2})$ and $I(^2P_{3/2})$, respectively.

Description of the Polarization Parameters. The probability of absorption of a photolysis photon by the molecule is proportional to $|\vec{\mu}\cdot\vec{\varepsilon}|$, where $\vec{\mu}$ is the transition dipole moment for excitation from the initial electronic state to the final excited state, and $\vec{\varepsilon}$ is the polarization direction of the linearly polarized photolysis light. In the absorption step, only those molecules with the axis conveniently oriented with respect to the photolysis electric field are excited, and thus, the product ensemble is produced with a certain degree of alignment along the polarization of the photolysis pulse if the photodissociation process is fast enough. For diatomic or polyatomic molecules with a well-defined molecular axis, parallel or perpendicular transitions can be referred to as the alignment of the molecular axis with respect to the transition dipole moment. The transition dipole moment is aligned along the molecular axis in a parallel transition while in a perpendicular transition it is located perpendicular to the molecular axis. When dissociation is faster than the molecular rotational period—like in a prompt dissociation—the fragments will recoil along the molecular axis, and the dissociation will be well described by the axial recoil limit. In these cases, the parallel or perpendicular character of the electronic transition will be directly reflected by maximum values of the anisotropy parameter. However, in polyatomic molecules with more than one main molecular axis, the dissociating bond might not be completely aligned or antialigned along the polarization direction of the photolysis laser, even for prompt dissociation. This is the case of the CH_2BrI molecule since the presence of two well-defined molecular axes, C−Br and C−I bonds, forming a Br−C−I angle around 114°, leads to transition dipole moments located in the Br−C−I plane, but often at a certain angle of both the C−Br and C−I bonds.[30] Therefore, no correlation can be drawn *a priori* between the transition character and the molecular axis.

For both the $Br(^2P_{3/2})$ and $I(^2P_{3/2})$ atoms, the ${a_0}^2(\|)$ parameter ranges from −0.8 to +0.8,[39] where the maximal positive and negative values would correspond to population of the corresponding atom in exclusively $m_J = \pm 1/2$ and $m_J = \pm 3/2$ states, respectively, with respect to the quantization axes, given by the Br and I atom recoil directions.

For parallel transitions there is no net change in the projection of the total angular momentum onto the bond axis. In a diatomic AB molecule, the preservation of the angular momentum implies that $m_J(A) + m_J(B) = 0$. Determination of the ${a_0}^2(\|)$ polarization parameter for one of the fragments provides, therefore, indirect similar information for the other. On the contrary, in those cases where the coproduct of the atomic fragments is a polyatomic, the angular momentum of both products is conditioned by the rotation of the latest, and no preferential population (alignment) is expected for the atomic species. As discussed in the following sections, any divergence from such expectance would aport significant dynamical information.

Theoretical Method. To shed light into the possible fragmentation pathways of CH_2BrI, high level *ab initio* calculations were performed to compute 1D potential energy curves (PECs) that connect the Franck−Condon region to three possible fragmentation channels: CH_2I + Br, CH_2Br + I, and CH_2 + IBr. All calculations were performed with the MOLPRO package[40] and the ANO-RCC-VQZP basis set was considered. For iodine and bromine, core pseudopotentials of 28 and 10 electrons, respectively, were employed. To obtain the geometries to build the PECs, several relaxed scans have been performed on the ground state at CASPT2 level,[41] where the reaction coordinate is fixed at several distances while the remaining coordinates are optimized. In total, four relaxed scans were performed: one where CH_2Br is relaxed as a function of the C−I distance, R_{CI}, the counterpart where CH_2I is relaxed as a function of the C−Br distance, R_{CBr}, and a roaming mechanism where the Br atom dissociates and strip the I atom to form IBr. Finally, a direct mechanism where the C−X distance is considered as the reaction coordinate, X being the geometrical center between the I and Br atoms. Since CH_2 in its ground state is a triplet state, for the two channels leading to IBr, both singlet and triplet states have been explored at large distances and a progressive transition in the geometries was considered to obtain a smooth ground state PEC. For each fragmentation path, 9 singlet states (5A′ and 4A″) and 9 triplet states (5A′ and 4A″) have then been computed at CASSCF/MRCI level[42] for

https://doi.org/10.1021/acs.jpca.2c05897
J. Phys. Chem. A 2022, 126, 8404−8422

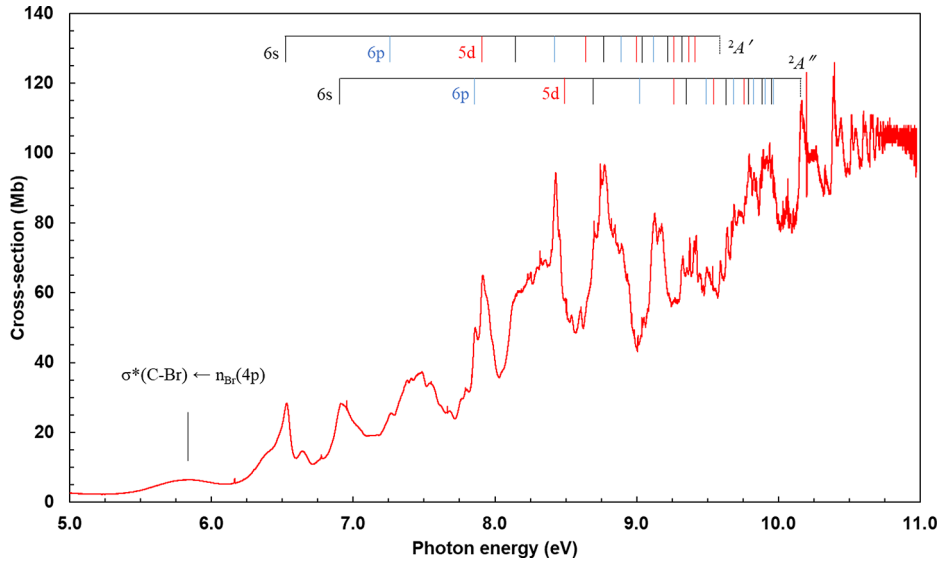

Figure 1. Gas-phase room-temperature high-resolution VUV photoabsorption spectrum of CH_2BrI (red line) in the 5−11 eV photon energy range. The spectrum presents tentative assignments of both valence and Rydberg states (see the text for more details).

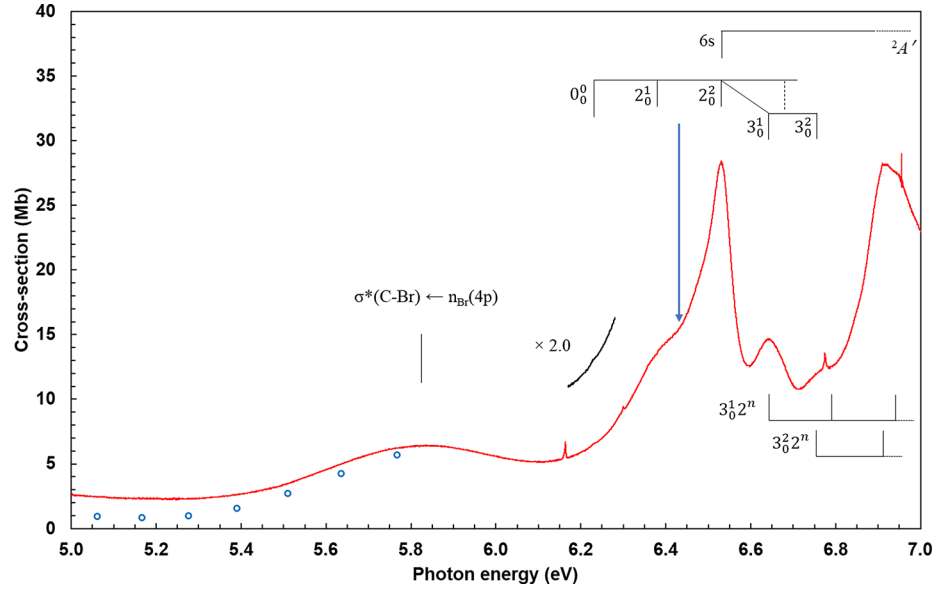

Figure 2. High-resolution VUV photoabsorption spectrum of CH_2BrI (red line) in the 5−7 eV photon energy range. The blue circles correspond to the VUV data of Mössinger et al.[6] The spectrum shows an assignment of both Rydberg states and vibrational levels. The vertical arrow indicates the excitation energy (wavelength), 6.424 eV (193 nm), used in the present photodissociation study. The narrow peaks at 6.163 and 6.774 eV correspond to methyl iodide, while the peak at 6.955 eV to atomic I from photolysis of the molecule (see SI).

approximately 30 geometries. The active space employed to generate the reference configurations consists of 20 electrons in 12 orbitals (9 a' and 3 a''), while 13 a' and 6 a'' orbitals where kept doubly occupied. Finally, spin−orbit matrix elements where calculated from the obtained MRCI electronic wave functions using the Breit−Pauli method implemented in MOLPRO,[43] and the 36 eigenvalues of the full spin−orbit matrix considered in this work were computed.

EXPERIMENTAL RESULTS

High-Resolution VUV Absorption Spectrum. The gas-phase room-temperature high-resolution VUV absorption spectrum of CH_2BrI (photoabsorption cross-section in units of Mb ≡ 10^{-18} cm^2), measured in the 5−11 eV photon energy range, is shown in Figure 1, while an expanded view of the energy region of interest in this work (5−7 eV) is depicted in Figure 2. More detailed sections corresponding to higher photon energies (7−11 eV) along with a detailed description of the identified features is included in the Supporting Information (SI) for the interested reader.

We have adopted the normal mode description and numbering from the vibrational analysis of Lee et al.[44] This includes, in particular, fine structure assignment to the CH_2 scissoring and wagging modes, ν_2' and ν_3', respectively, with ground state energies of 1374 cm^{-1} and 1150 cm^{-1},[7] along with the contribution of C−Br stretching ν_4', C−I stretching ν_5', and Br−C−I bending ν_6' modes, with ground state energies of 616 cm^{-1}, 517 cm^{-1}, and 144 cm^{-1}, respectively. The absorption bands are classified as excitations from the ground state to

https://doi.org/10.1021/acs.jpca.2c05897
J. Phys. Chem. A 2022, 126, 8404−8422

valence states, but mainly with Rydberg character. For the assignments of the vibronic structure, we use the notation X^n_m, with m and n being the initial and final vibrational states, respectively, while X denotes the particular geometric change the molecule undergoes in the photoabsorption process.

The 5−7 eV Photon Energy Range. The first absorption band, the so-called *A*-band, lying in the 4−5 eV energy range is assigned to the σ^*(C−I) ← n_I(5p) transition (not shown in the spectra of Figures 1 and 2). A first weak structureless band peaking at 5.837 eV (∼212 nm) is observed in Figures 1 and 2 and assigned to the σ^*(C−Br) ← n_{Br}(4p) transition (*i.e.*, $9A' \leftarrow \tilde{X}^1A'$ based on the high-level *ab initio* calculations carried out in the present work—see below). As in our previous work,[21] this band is referred to as the A' band. This band has been previously reported[6,7,10,45−48] where a general agreement is noted for its maximum position, yet the absolute cross-section values in the wavelength range 215−250 nm (5.767−4.959 eV) of Mössinger et al.[6] are 9−35% lower than the present high-resolution data (see Figure 2). Additionally, this band has been also the subject of experimental[7,46,48] and theoretical[10,47,48] photodissociation dynamics studies, with relevant information about the energies of the activated vibrational modes.

The second feature observed peaking at 6.529 eV (∼190 nm), with a local cross-section value of 28.2 Mb, can be assigned to the lowest lying 6s Rydberg transition from the iodine nonbonding n_I(5p) lone pair converging to the lowest ionic−electronic ground state ($2A'$). In agreement with the present calculations (see below), a partially overlapped valence transition is observed with its vertical value tentatively placed also at 6.529 eV. We have assigned this to the σ^*(C−Br) ← n_{Br}(4p) (*i.e.*, $13A' \leftarrow \tilde{X}^1A'$) transition. The 0^0_0 origin band is tentatively assigned at 6.23(2) eV. The modest fine structure observed is attributed to vibrational excitation as identified in Table S3 of the ESI. A 2^n_0 (n = 0−3) progression of the CH_2 scissoring mode, ν_2', is identified with an average spacing of 0.154 eV (1242 cm^{-1}), although a contribution from the CH_2 wagging mode, ν_3', is also discernible. Notice that excitation in the present work is at 193 nm (6.424 eV), as indicated by the vertical arrow in Figure 2, therefore at about the 2^1_0 vibronic band of the $13A' \leftarrow \tilde{X}^1A'$ transition.

Above 7 eV Photon Energy Range. The photoabsorption spectrum above 7 eV displays prominent Rydberg features (see Figure 1), while based on the present calculations, a valence transition is predicted at 8.04 eV. The experimental vertical value is at 7.488 eV (with a cross-section of 37.2 Mb), in reasonable agreement with the calculation given the level of accuracy used (±0.5 eV), and is assigned to the $17A' \leftarrow \tilde{X}^1A'$ transition. Given the background contribution to the absorption band, the nature of this transition is reminiscent of a dissociative character. We are not aware of any other information in the literature to compare with the present finding. The lowest-lying Rydberg series is assigned to the promotion of iodine nonbonding n_I(5p) lone pair electron to an *ns* Rydberg orbital, with the first member for n = 6 at 6.529 eV and an effective quantum number n^* = 2.11 while extending up to n = 11. Similar *np* and *nd* Rydberg series converging to the lowest cationic electronic state, $2A'$, lying at 9.5944 eV[44] are also identified, with the first members for n = 6 and n = 5, respectively, lying at 7.27(4) eV and 7.922 eV (with n^* = 2.42 and 2.85). The modest fine structure observed for the first members of the three Rydberg series can be assigned to different vibrational modes, i.e., CH_2 scissoring and wagging, ν_2' and ν_3', C−Br stretching ν_4' and C−I stretching ν_5' modes. More detailed information, including a full assignment, can be found in the SI. Also *ns*, *np*, and *nd* Rydberg series converging to the second ionization energy at 10.1644 eV,[49] corresponding to the $2A''$ ionic state, have been identified. The first members of these series are associated with features at 6.913 eV (n^* = 2.05), 7.866 eV (n^* = 2.43) and 8.49(9) eV (n^* = 2.86). The present Rydberg (tentative) assignments have been made up to n = 12 for the *ns* and *np* series (see the SI for detailed information). The observed fine structure in these absorption peaks has been similarly assigned to vibrational excitation involving the CH_2 scissoring ν_2', the CH_2 wagging ν_3', the C−Br stretching ν_4', the C−I stretching ν_5', and the Br−C−I bending ν_6' modes.

Photodissociation Dynamics and Atomic Photofragment Alignment. *Br*($^2P_{1/2}$) and I*($^2P_{1/2}$) Ion Images.* Figure 3 shows 2D slice ion images of Br*($^2P_{1/2}$) and I*($^2P_{1/2}$) produced in the photodissociation of CH_2BrI at 193 nm. Three different features can be distinguished in the Br*($^2P_{1/2}$) image, namely, a central intense oval-shaped disc, assigned to multiphoton ionization (MPI) and statistical decay, and two highly anisotropic rings of different radii. A careful inspection of the I*($^2P_{1/2}$) image, whose overall signal is significantly lower than that of Br*($^2P_{1/2}$), brings to light three features, quite similar to those observed for the Br* fragment. Since in the original I*($^2P_{1/2}$) image, the outermost contribution was highly obscured by the intense and unstructured central blot to obtain a good visualization of the rings, the intensity of the external feature has been amplified with respect to the central one by a factor of 2. The polarization of the pump and probe lasers were set mutually parallel and with respect to the detection plane, as indicated by the red arrows on the top right corner of the image (*XX* images).

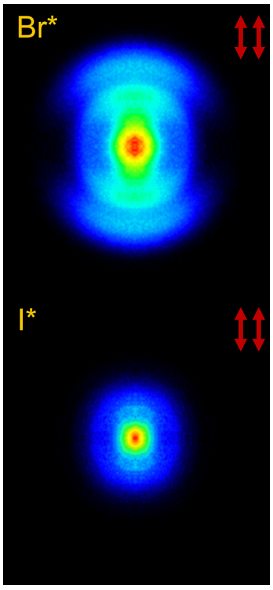

Figure 3. Symmetrized slice ion images of the Br*($^2P_{1/2}$) and I*($^2P_{1/2}$) fragments produced in the photodissociation of CH_2BrI at excitation wavelength λ = 193 nm, detected by (2 + 1) REMPI at 262.45 and 305.49 nm, respectively. The external ring in the I* image has been increased by a factor of 2 with respect to the central feature for better visualization. The red arrows show the polarization of the pump (left) and probe (right) lasers.

https://doi.org/10.1021/acs.jpca.2c05897
J. Phys. Chem. A 2022, 126, 8404−8422

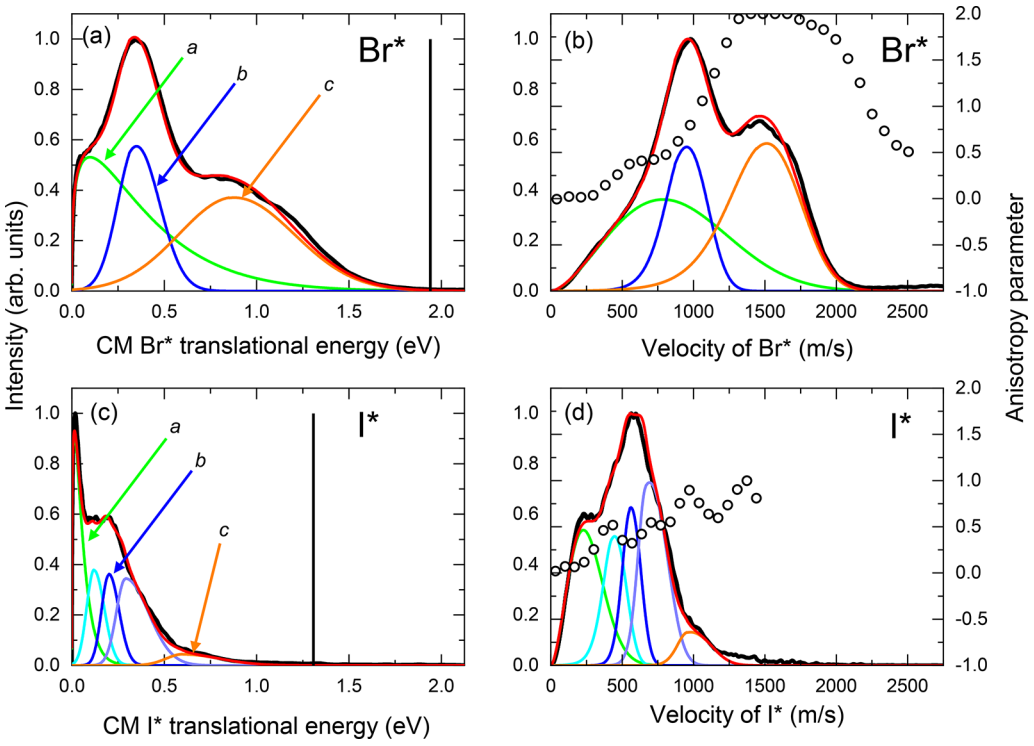

Figure 4. (a, b) Center-of-mass (CM) translational energy and velocity distributions for the Br*($^2P_{1/2}$) fragment, respectively, represented by the black curve. The color lines correspond to three contributions obtained in the deconvolution—labeled *a*, *b* and *c*—wherein the red curve comprises the overall fit. (c, d) The black curve corresponds to the experimental translational energy and velocity distributions for the I*($^2P_{1/2}$) fragment, while the green, blue-ish, and orange represent the different *a*, *b*, and *c* contributions. The black vertical lines in the energy distributions represent the available energy for the main dissociation process. The black circles in the velocity distributions correspond to the anisotropy β parameter.

The translational energy distributions (TEDs) obtained from the angular integration of the Br*($^2P_{1/2}$) and I*($^2P_{1/2}$) slice images are presented in Figure 4a and 4c. Both distributions depict reasonably well the features observed in the images, *i.e.*, a very low-recoil peak—a shoulder in the case of Br*—a central peak (which will be later on attributed to prompt C−X bond breaking) and a high kinetic energy contribution, the later one concealed in the tail of the I* TED. Despite the similarities between both distributions for the Br*($^2P_{1/2}$) and I*($^2P_{1/2}$) photofragments, the differences in intensity and in shape are evident. With the aim of identifying the possible channels and the underlying dynamics giving rise to the observed features, the experimental profiles have been fitted to a series of mathematical functions.

The low-recoil peak was fitted to a simplified Muckerman distribution[50]

$$I(E_k) = AE_k^i(1 - E_k)^j \quad (7)$$

represented by green lines in Figure 4a and 4c, where E_k is the translational (kinetic) energy of the fragment, and *A*, *i*, and *j* are fitting parameters that do not contain any specific physical meaning. Muckerman functions are widely used to reproduce Boltzmann-like profiles, *i.e.*, contributions from statistical processes.[50] Gaussian functions were used, on the other hand, to fit the other two contributions (blue-ish and orange lines in Figure 4a and 4c). The broad and unstructured peaks in the Br* TED (Figure 4a) were satisfactorily reproduced by two Gaussian distributions peaking at 0.31 eV (full-width-half-maximum, fwhm = 0.23 eV) and 0.88 eV (fwhm = 0.63 eV), respectively; the Muckerman function for the low-recoil contribution peaked at ∼0.1 eV.

Moreover, as in the case of Br*, a Muckerman and a Gaussian function were used to reproduce the low and high energy contributions of the I* TED (Figure 4c), located at <0.1 and 0.6 eV (fwhm = 0.29 eV), respectively, corresponding to the central and outermost contributions of the I* image (Figure 3). The central contribution in the TED of the I* product, however, appears as a plateau which shows a clear structure reminiscent of vibrational activity in the CH_2Br coproduct; a set of three Gaussians were tentatively used to reproduce the observed structure.

For the sake of clarity, the slow-recoil, the intense middle and the fast contributions were labeled *a*, *b*, and *c*, respectively. The deconvolution analysis of the Br* and I* distributions into three different components, as described above, is amply justified by three relevant arguments. First, the results depicted in Figure 4 are similarly reproduced when certain experimental conditions, such as the laser power and the temperature of the molecular beam, were varied; second, these three contributions have been previously reported at other excitation wavelengths by different authors, including our previous work on the CH_2BrI photodissociation from the *A* and *A*′ bands;[21] third, the measured photofragment polarization discussed hereafter supports the existence of the three contributions.

Through radial integration of the images shown in Figure 3, the corresponding angular distributions (not shown in this work) were obtained. The subsequent analysis using eq 1 produces the speed-dependent anisotropy β parameter shown in Figure 4b and 4d. From the evolution of the β parameter with the velocity (v) of the fragment, the existence of three dynamical regions can be presumed, corroborating the deconvolution analysis presented previously. For the Br* fragment, $\beta(v)$ can be

https://doi.org/10.1021/acs.jpca.2c05897
J. Phys. Chem. A 2022, 126, 8404−8422

visualized as a step function, showing quite clearly three dynamical regions. At low Br* velocities, the anisotropy parameter takes values close to zero; at velocities ∼500 m/s, β increases abruptly up to $\beta \simeq 0.5$. The second plateau lasts until v ∼ 1100 m/s where a second sudden change takes the anisotropy parameter to $\beta = 2$, the maximum value for a pure parallel transition. The following decay is due to the signal intensity decrease. It must be warned that neither the frontiers where the change is produced, nor the values obtained for the anisotropy parameter should be taken as absolute references. Clearly, the overlap between the three contributions to the overall process must alter both numerical results. A strong confirmation of three dynamical regions and relatable valuable information can be extracted nevertheless, as it will be discussed in following sections.

A similar, although somehow more complicated picture can be extracted from Figure 4d, corresponding to the I* fragment. Impressively, the differences in the behavior of the anisotropy parameter in Figure 4d with respect to that observed in Figure 4b can be straightforwardly related to the differences observed both in nature and ratio of the deconvolution analysis. In the velocity region dominated by the low-recoil component (a contribution), the β parameter takes values close to zero. At velocities ∼500 m/s, the value increases but, instead of reaching a plateau, the value oscillates between $\beta \sim 0.3$ and 0.6; it is not a coincidence that the velocity distribution—or the TED, by all means—in this region (b component) shows a vibrational-like structure and ought to be fitted using a set of three Gaussian functions. For velocities above ∼1000 m/s, the anisotropy parameter increases to a maximum value of $\beta \sim 1$, although the oscillatory behavior persists. Wether the reduced value of β should be related to the nature of contribution c or to the branching ratio between the b and c components, will be later on discussed in detail. It must be mentioned in this moment, however, that the results obtained for the $I(^2P_{3/2})$ species will cause a partial reinterpretation of the deconvolution analysis performed for the $I^*(^2P_{1/2})$ product.

$Br(^2P_{3/2})$ and $I(^2P_{3/2})$ Ion Images. Figures 5 and 6 show the 2D slice images and the corresponding translational energy distributions for the $Br(^2P_{3/2})$ and $I(^2P_{3/2})$ fragments produced in the photodissociation of CH_2BrI at 193 nm. Since the $Br(^2P_{3/2})$ and $I(^2P_{3/2})$ atoms may show polarization effects, as discussed later, images in the four *XX*, *XZ*, *ZX*, and *ZZ* configurations were acquired. The direction of the pump and probe laser polarizations is indicated in each image by red arrows (parallel polarization) and dots and circles (perpendicular polarization) on the top right corner.

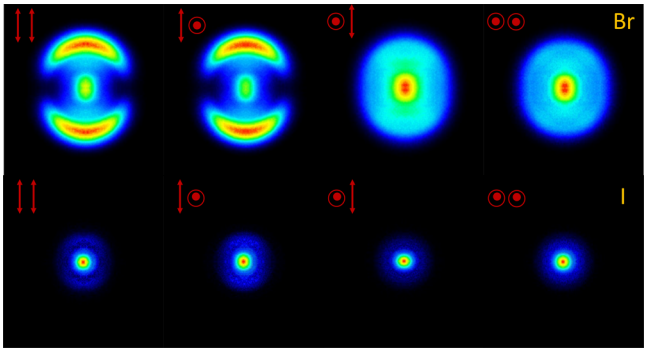

Figure 5. Symmetrized slice ion images of the $Br(^2P_{3/2})$ and $I(^2P_{3/2})$ fragments produced in the photodissociation of CH_2BrI at excitation wavelength λ = 193 nm, detected by (2 + 1) REMPI at 250.35 and 304.58 nm, respectively. The external ring in the I images has been increased by a factor of 3 with respect to the central feature. The red arrows show the polarization of the pump (left) and probe (right) lasers.

Only two different features can be distinguished in the $Br(^2P_{3/2})$ and $I(^2P_{3/2})$ images; specifically, a highly anisotropic ring and a central intense low-recoil disc assigned to MPI and statistical processes. As in the case of Br* and I*, the overall signal recorded for the iodine atom is significantly lower than that of the bromine atom. Despite the qualitative coincidences, the images of the I fragment differ strongly from those obtained for the Br atom both in size and in the intensity ratio of the two features. The color pattern in the $I(^2P_{3/2})$ images was altered, as before, to enhance the visualization of the external ring, whose intensity was multiplied by a factor of 3 with respect to the central feature. The ring displays parallel anisotropy, although not as strongly as in the bromine case.

The TEDs shown in Figure 6a and 6c reproduce the observed features in the images, although the existence of an additional contribution in both cases can be guessed. As in the case of Br* and I*, a deconvolution analysis was carried out to uncover all possible contributions to the experimental profile. The analysis provides, indeed, three contributions for both fragments. The slow-recoil contribution, peaking at less than 0.1 eV is clearly visible in both cases—constituting the dominant feature in the I TED—and is well reproduced by a Muckerman function. The intense and broad peak at 0.80 eV (fwhm = 0.48 eV), which dominates the TED of the Br atom shows a glimpse of a minor contribution at lower kinetic energy values. The analysis shows that the TED is well reproduced by two Gaussian functions (besides the mentioned Muckerman function), and allows us to locate the middle contribution at 0.35 eV with a fwhm of 0.38 eV. The I TED shows a hint as well of a third contribution, this time located at higher kinetic energy values than that of the main feature of the profile. The analysis shows, once more, that the TED profile is well reproduced by three contributions, the said Muckerman function (a contribution) and two Gaussian functions, that is to say, a middle one located at 0.26 with a fwhm of 0.24 eV (b contribution) and week higher-recoil peak located at 0.60 eV with a fwhm of 0.30 eV (c contribution).

According to eq 6a, the analysis of the photofragment polarization for the $Br(^2P_{3/2})$ and $I(^2P_{3/2})$ fragments requires the additional measurement of the *XZ* and *ZX* images. The images acquired at the various configurations of the pump and probe laser polarizations comprise different amount and type of information. The *XX* image, for instance, gathers all the data derived from both the dissociation and detection processes; the polarization of the probe laser in the *XZ* images is aligned perpendicular to the detection plane and, therefore, the information relative to the detection of the fragments is lost. The *ZX* image, on the other hand, cannot be related to the anisotropy of the dissociation step. A preliminary inspection of the images, might, therefore, shed some light onto the photofragment polarization in the form of atomic photofragment alignment.

The *XX* and *XZ* images recorded for the Br fragment present quite similar shapes with no observable differences between them. This fact suggests a minor photofragment alignment or, in other words, that the stereodynamics of the photodecomposition process is governed by the dissociation anisotropy. The differences between the *XX* and *ZX* images should inform on the photofragment polarization evinced by the detection process. In

https://doi.org/10.1021/acs.jpca.2c05897
J. Phys. Chem. A 2022, 126, 8404−8422

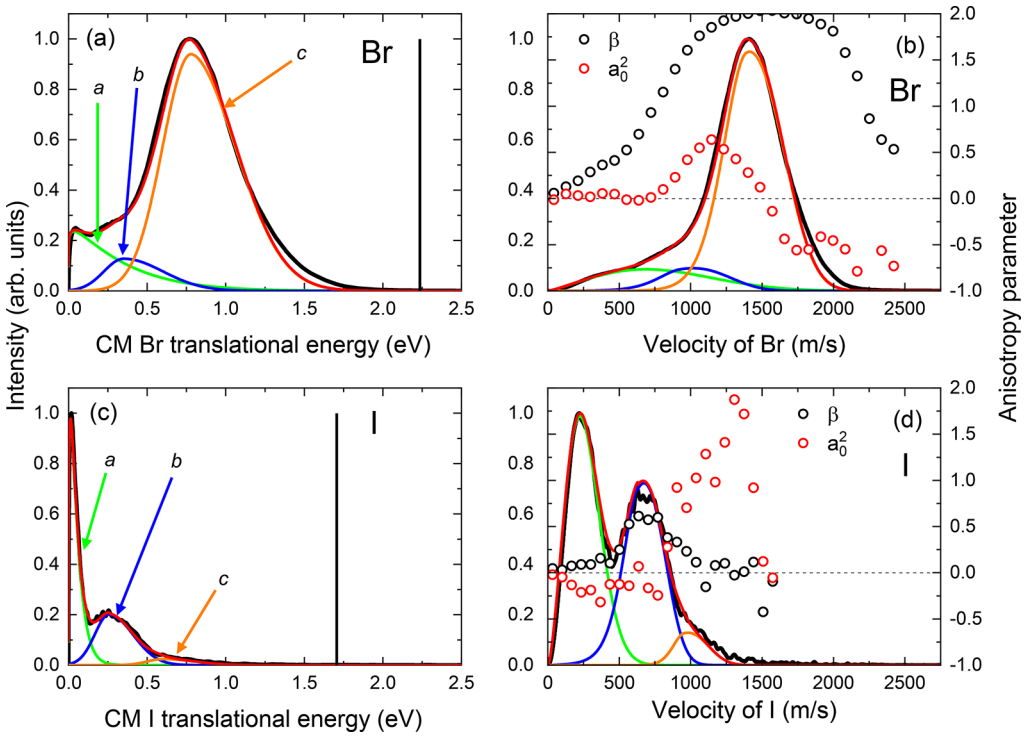

Figure 6. (a, c) Center-of-mass (CM) translational energy distributions for the Br($^2P_{3/2}$) and I($^2P_{3/2}$) fragments, respectively, represented by black curves. The green, blue, and orange lines correspond to three contributions obtained in the deconvolution analysis—labeled, respectively, *a*, *b*, and *c*—while the red curve is the overall fit. (b, d) Velocity distributions of the same fragments. The black circles correspond to the anisotropy β parameter, while the red circles correspond to the $a_0^2(\|)$ alignment parameter. The green, blue, and orange lines correspond to three different contributions in the photodissociation process, while the red curve is the overall fit.

those cases, such as the current one, where the dissociation anisotropy dominates the stereodynamics, the specificity of the *ZX* image becomes more evident when compared to the *ZZ* image. The *ZZ* image does not comprise any dynamical information, and therefore, any anisotropic deviation must be integrated in the apparatus function. Consequently, if no photofragment polarization were expected, the *ZX* and *ZZ* images should look alike. The differences observed, explicitly, a weak anisotropic feature between the central spot and the outer ring, suggest that minor but non-negligible photofragment polarization is manifested in the detection process.

As before, the comparison between the iodine *XX* and *XZ* images emphasizes the predominance of the dissociation process on the photofragment polarization. The strong similitude between the *ZX* and *ZZ* images suggests, on the other hand, that there are no polarization effects that could be brought to the surface by the detection process.

Through radial integration of the images shown in Figure 5, the corresponding angular distributions (not shown in this work) were obtained. The subsequent analysis using eq 6aresults in the speed-dependent anisotropy β and alignment $a_0^2(\|)$ parameters shown in Figure 6b and 6d. From the evolution of β with the velocity of the fragment, the existence of three dynamical regions is confirmed. It must be stated that the analysis included the $Re[a_1^2(\|, \perp)]$ parameter, but no deviations from $Re[a_1^2(\|, \perp)] \approx 0$ were found.

The behavior of the β parameter throughout the Br profile turns out to be highly conditioned by the predominant *c* contribution and obscures the anisotropy values anticipated for the other two contributions. On the light shed by the analysis performed for the Br* fragment, however, some information can be extracted. In the low recoil velocity region ($v \leq 500$ ms^{-1}), the β parameter increases almost linearly from zero to ~0.4. From 500 to 1500 ms^{-1}, the anisotropy increases up to $\beta = 2$, in coincidence with the maximum of the distribution. The wide overlap between the *a* and *b* contributions distorts the step-like behavior observed for the Br* fragment, but it might safely be concluded a $\beta \simeq 0$ for the low-recoil component and a β somewhat higher, closer to 0.5, for the *b* component. The *fast c* contribution shows, as before, the maximum value corresponding to a perpendicular transition.

The variations of the $a_0^2(\|)$ alignment parameter throughout the Br profile can be, on the other hand, clearly associated with the three dynamical regions. For the low-recoil contribution, $a_0^2(\|) = 0$; a maximum value of ~0.7 is obtained at $v \simeq 1250$ ms^{-1}, coincident with the maximum of the *b* contribution, from were, $a_0^2(\|)$ decreases down to ~−0.6. The strong overlap between the *b* and *c* curves suggests that the real value of the $a_0^2(\|)$ parameter corresponding to the *b* contribution must be larger by far than the observed maximum of ~0.7. In addition, the registered change of sign indicates two rather different dynamical sources for the *b* and *c* contributions.

The dependence of the β parameter on the velocity of the I($^2P_{3/2}$) fragment indicates that some similar conclusions are applicable to this case, which can be summarized as follows: At low recoil velocities, the TED is dominated by an isotropic contribution ($\beta = 0$), which is coherent with a stochastic dynamics; in the middle region, the predominant parallel contribution is characterized by a anisotropy value of ≃0.5−0.6. At higher velocities, however, a clear discrepancy with the previous cases reveals and forces, in addition, a partial

https://doi.org/10.1021/acs.jpca.2c05897
J. Phys. Chem. A 2022, 126, 8404−8422

reinterpretation of the analysis performed for the I*($^2P_{1/2}$) fragment (see above). The β parameter in the region corresponding to the *c* contribution of Figure 6d clearly decreases to zero. This fact points toward a different overall dynamics for the source of this component in the I(^2P_J) TEDs than that behind the same component in the Br(^2P_J) (with $J = 3/2$ and 1/2 for Br/I and Br*/I*, respectively) distributions. Assuming a concomitant dynamics for formation of I($^2P_{3/2}$) and I*($^2P_{1/2}$), the average values of $\beta \sim 0.8$ and the oscillatory behavior observed in the high energy region of Figure 4d suggest a wider *b* contribution than that originally assumed, which should include the orange Gaussian function, initially interpreted as the third, *c* contribution. An additional conclusion of this interpretation is a minor or negligible contribution to the I signal, in this case, of the process behind the *c* component of the TED.

The maximum translational energies—associated with the total available energy, E_{av}—for the dissociation products are represented in panels a and c of Figures 4 and 6 as black vertical bars. The E_{av} values were derived from the energy balance for the photodissociation of CH_2XY (where *X* and *Y* represent either halogen atom) in the following way:

$$E_{av} = h\nu - D_0(CH_2X - Y) - E_{SO}(Y) + E_{int}(CH_2XY) \quad (8)$$

where $h\nu$ represents the excitation photon energy; $D_0(CH_2X-Y)$ is the C−Y bond dissociation energy, which takes values of 2.936 and 2.389 eV[8] for $CH_2I(\tilde{X})$−Br and $CH_2Br(\tilde{X})$−I channels, respectively; $E_{SO}(Y)$ is the spin−orbit splitting of the Br(^2P_J) and I(^2P_J) atoms (for I and Br, $E_{SO} = 0$; and E_{SO}(Br*) = 0.460 eV and E_{SO}(I*) = 0.943 eV). The term $E_{int}(CH_2XY)$ corresponds to the internal energy of the parent molecule, which, under molecular beam conditions, might be considered negligible.

THEORETICAL RESULTS

The vertical excitation energies and respective total transition dipole moments (TDM) are presented in Table 1. The TDMs along each axis are also included. The *X* axis is located perpendicular to the Br−C−I plane, while the *Y* and *Z* axis are in the plane, *Y* being perpendicular to C−Br and pointing roughly between Br and I, and *Z* being parallel to Br−I. We note that *A*″ states are characterized as expected by a TDM along the *X* axis, *i.e.*, perpendicular to the Br−C−I plane, while *A*′ states are associated with TDM components in the *Y* and *Z* axis, *i.e.*, in the plane.

The results are in good agreement with recent previous results,[21] although the vertical excitation energies obtained here are somewhat larger, around 0.4 eV above. The present calculations include a larger active space in order to properly describe higher excited states and, in particular, those absorbing around 193 nm, in the third absorption *B*-band.

The first excited states characterize the *A* band, where a major absorption into the 5*A*′ state is expected along with some contribution of the 4*A*′ and 4*A*″ states. At higher energies, we note the noticeable excitation of the 9*A*′ state, characteristic of the *A*′ band lying around 210 nm. At the highest energies, in particular at 193 nm, major absorption into the 13*A*′ state is expected, in agreement with the reported absorption spectrum (see Figure 2).

The potential energy curves (PECs) as a function of the C−Br and C−I distances are depicted in Figures 7 and 8, respectively. The first excited states, in particular the 4*A*′, 4*A*″, 5*A*′, and 5*A*″

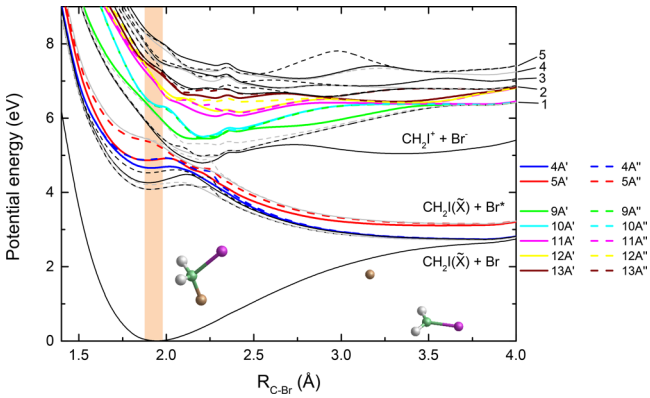

Figure 7. Computed CASSCF/MRCI potential energy curves for the CH_2I + Br channel of CH_2BrI relaxing the CH_2I moiety in the ground state using CASPT2. The solid lines correspond to the *A*′ symmetry levels while the dotted lines correspond to the *A*″ symmetry. Colored curves correspond to the representative excited states. The shaded area indicates the Franck−Condon region. Numbered asymptotes are as follows: (1) $CH_2I(\tilde{A})$ + Br; (2) $CH_2I(\tilde{A})$ + Br*; (3) $CH_2I(\tilde{B})$ + Br; (4) $CH_2I(\tilde{C})$ + Br; (5) $CH_2I(\tilde{B})$ + Br*.

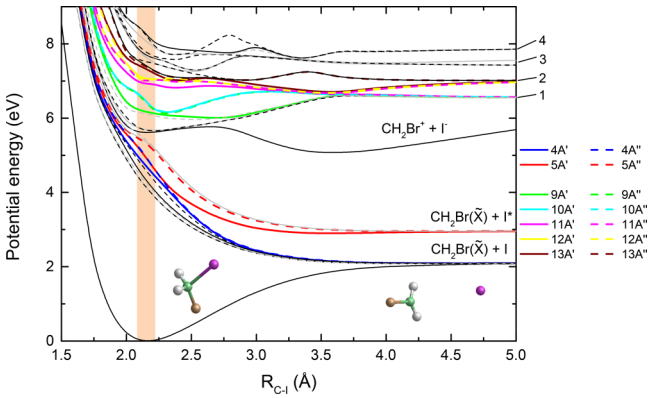

Figure 8. Computed CASSCF/MRCI potential energy curves for the CH_2Br + I/I* channels of CH_2BrI relaxing the CH_2Br moiety in the ground state using CASPT2. The solid lines correspond to the *A*′ symmetry levels while the dotted lines correspond to the *A*″ symmetry. Colored curves correspond to the representative excited states. The shaded area indicates the Franck−Condon region. Numbered asymptotes are as follows: (1) $CH_2Br(\tilde{A})$ + I; (2) $CH_2Br(\tilde{B})$ + I; (3) $CH_2Br(\tilde{A})$ + I*; (4) $CH_2Br(\tilde{B})$ + I*.

states, present a highly repulsive shape along the C−I distance (see Figure 8), as expected for the *A* band, which is related to the C−I bond cleavage.

We notice that the present PECs correspond to the adiabatic representation. In Figure 7, a clear avoided crossing is observed between these first excited states (4*A*′, 4*A*″, 5*A*′, and 5*A*″) and higher excited states including the 9*A*′. In the diabatic representation, the first excited states, associated with the *A*-band, are indeed characterized by a bound shape along the C−Br distance while higher excited states, in particular the 9*A*′ state, present a purely repulsive shape along this coordinate. This is consistent with the structureless continuum observed in the absorption spectrum associated with the *A*′-band. At higher energies, the 13*A*′ state presents a rather bound shape along both the C−I and C−Br distances, in agreement with the measured absorption spectrum, characterized by well-defined vibrational progressions. In Figure 7, two avoided crossings are clearly observed allowing dissociation: from 13*A*′ to 11*A*′/11*A*″

https://doi.org/10.1021/acs.jpca.2c05897
J. Phys. Chem. A 2022, 126, 8404−8422

or $12A'/12A''$ and then into $10A'/9A''$. In contrast, direct elimination of iodine seems unlikely since no avoided crossings are observed in the proximity of the Franck−Condon region.

Figures 9 and 10 show possible pathways to produce CH_2 + IBr, which is a product channel accessible energetically.[8,20]

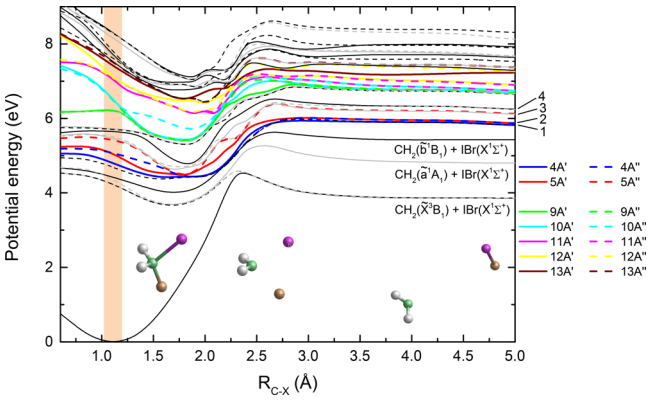

Figure 9. Computed CASSCF/MRCI potential energy curves for the direct formation of CH_2 + IBr, where the C−X distance is considered as the reaction coordinate, X being the geometrical center between the I and Br atoms. The solid lines correspond to the A' symmetry levels while the dotted lines correspond to the A'' symmetry. Colored curves correspond to the representative excited states. The shaded area indicates the Franck−Condon region. Numbered asymptotes are as follows: (1) $CH_2(\tilde{X}^3B_1)$ + IBr($A^3\Pi(2)$); (2) $CH_2(\tilde{X}^3B_1)$ + IBr($A^3\Pi$-(1)); (3) $CH_2(\tilde{X}^3B_1)$ + IBr($B^3\Pi(0^+)$); (4) $CH_2(\tilde{X}^3B_1)$ + IBr($C^1\Pi(1)$).

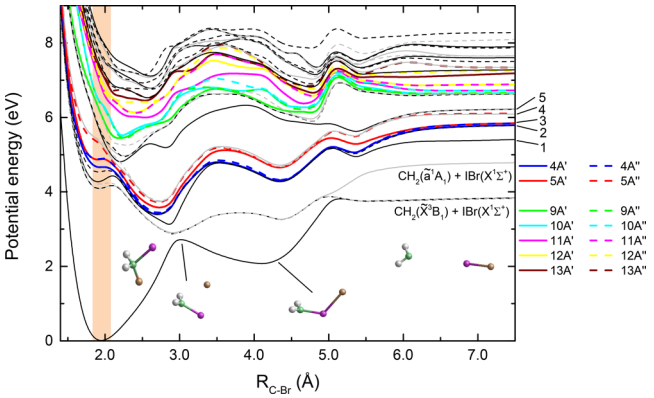

Figure 10. Computed CASSCF/MRCI potential energy curves for the isomerization after elongation of the C−Br bond, yielding CH_2−I−Br and finally breaking to CH_2 + IBr. The solid lines correspond to the A' symmetry levels while the dotted lines correspond to the A'' symmetry. Colored curves correspond to the representative excited states. The shaded area indicates the Franck−Condon region. Numbered asymptotes are as follows: (1) $CH_2(\tilde{b}^1B_1)$ + IBr($X^1\Sigma^+$); (2) $CH_2(\tilde{X}^3B_1)$ + IBr($A^3\Pi(2)$); (3) $CH_2(\tilde{X}^3B_1)$ + IBr($A^3\Pi(1)$); (4) $CH_2(\tilde{X}^3B_1)$ + IBr($B^3\Pi(0^+)$); (5) $CH_2(\tilde{X}^3B_1)$ + IBr($C^1\Pi(1)$).

Figure 9 shows the PECs associated with the symmetric stretch of both C−I and C−Br bonds, in terms of the C−X reaction coordinate, where X is the geometrical center between the I and Br atoms. These PECs provide us with possible pathways for direct dissociation into CH_2 + IBr upon excitation of the parent molecule at 193 nm. As can be seen, even if not completely forbidden, this mechanism is very unlikely since all electronic states show significant barriers in the C−X coordinate, while the elimination of Br is barrierless and straightforward, which explains the very low yields of the IBr and CH_2 fragments observed experimentally.[8,20] However, the symmetric stretch of both bonds may induce electronic relaxation to lower electronic states, in particular to the $7A'$, and may explain a very minor elimination of IBr. In this work we tried to detect $CH_2(\tilde{X}^3B_1)$ by (2 + 1) REMPI at 311.8 nm[51] without success. Although it is predicted in ref.[51] that the REMPI transition is weak and only low vibrational energies of the $CH_2(\tilde{X}^3B_1)$ fragment would be detected, which makes detection of this fragment, if present, rather difficult, it is also clear from the present calculations that production of ground state $CH_2(\tilde{X}^3B_1)$ in correlation with IBr is very unfavorable.

Finally, Figure 10 shows that an isomerization mechanism, where first the Br atom is expelled and then strip the I atom to form CH_2−I−Br and later on CH_2 + IBr, cannot be excluded. However, here again, all electronic states exhibit barriers in the reaction path to reach the CH_2 + IBr channel, while Br-atom elimination is barrierless. Therefore, formation of IBr, even if energetically allowed, appears to be dynamically unfavorable, and if it occurs, it is expected to be very minor and very hard to detect.

■ ANALYSIS AND DISCUSSION

In this section, the main experimental results will be further analyzed and discussed benefiting from the PECs computed as a function of the C−Br and C−I distances. The velocity map images along with the corresponding TEDs show three different contributions for the four fragments.

- Contribution *a*, slow-recoil Boltzmann-type structure which is assigned to multiphoton ionization processes in all cases.
- Contribution *b*, Gaussian-type contribution at intermediate translational energies which is associated with prompt dissociation upon one-photon excitation.
- Contribution *c*, Gaussian-type contribution at larger translational energies which is particularly observed for the Br/Br* fragments. As further discussed below, it can be assigned to secondary dissociation upon a second photon absorption. This contribution is almost indiscernible in the measured TEDs for the I/I* fragments. The anisotropy analysis clearly demonstrates that the contribution observed at larger translational energies for I* fragment, initially labeled *c*, is indeed part of the prompt dissociation process−contribution *b*.

The prompt dissociation mechanisms leading to C−Br and C−I bond cleavage are discussed first, while the secondary dissociation upon a second-photon absorption is then explored.

Direct Dissociation Processes. *The Br(^2P_J) + CH_2I Channels.* The most remarkable information provided by the present work is the similarity between the experimental results obtained at 193 nm (excitation energy of 6.424 eV, assigned to the 2^1_0 vibronic band of the $13A' \leftarrow \tilde{X}^1A'$ transition−see above), with those previously obtained at 266 and 210 nm for dissociation into Br(^2P_J) from the A and A' bands, respectively.[21]

In the mentioned work, the experimental TEDs for both spin−orbit Br(^2P_J) atoms were analyzed and interpreted in terms of three contributions. A low-recoil, Boltzmann-like contribution was assigned to REMPI-assisted multiphoton dissociative ionization. The *middle* contribution (translational energy of 0.25 eV at 266 nm and 0.5 eV at 210 nm), which constituted the main result,[21] was assigned, in the case of

https://doi.org/10.1021/acs.jpca.2c05897
J. Phys. Chem. A 2022, 126, 8404−8422

excitation at 266 nm (A band), to indirect dissociation via absorption to the $5A'$ state and subsequent curve crossing with upper excited dissociative states such as the $9A'$, while upon excitation at 210 nm (A' band), it was attributed to direct dissociation in the $9A'$ excited state. A third broad and faster contribution was tentatively interpreted in terms of secondary dissociation of the CH_2Br fragment upon an additional one-photon absorption. At 210 nm, no $I(^2P_J)$ signals were detected, and the experimental observation of $I(^2P_J)$ at 266 nm were plainly rationalized in terms of a single fast decomposition process through direct absorption and ulterior dissociation through the $5A'$ state for the I fragments, and $5A' \rightarrow 4A'/4A''$ nonadiabatic crossing for the I* fragments.[21]

The prompt dissociation mechanism for both $Br(^2P_J)$ (at 266 and 210 nm) and $I(^2P_J)$ (at 266 nm) species were characterized by a large vibrational and rotational excitation in the polyatomic coproduct, with no thermal distribution of rotational states. In the corresponding translational energy distributions, such energy partitioning is revealed by a significant shift between the rise of the distributions and the available energy. The observed energy distribution was explained in terms of the soft impulsive model, developed by Bush and Wilson[52] and improved by Butler and co-workers.[53] The soft impulsive model predicts the energy partitioning among the different degrees-of-freedom (DOF) of the products of a photodissociation process interceded by a high repulsive electronic surface. The CH_2BrI, in particular, is well described by the soft radical version of the model, where the majority of the available energy (~50%) is transformed into rotational excitation of the CH_2Br or CH_2I fragments;[52,53] the energy channeled into translation adds up to ~20% of the available energy and the remaining ~30% should be transformed into vibrational excitation of the polyatomic fragments. This was confirmed by high-level *ab initio* electronic structure calculations and full dimension on-the-fly trajectory calculations including surface hoping,[22] where an *anchor* effect due to the remaining halogen atom in the dissociating parent molecule imparts significant rotational motion and leads to a remarkable rotational energy of the nascent cofragment.

It should be noticed that the fraction of the available energy transferred into the vibrational modes of the polyatomic products is not explicitly predicted by the soft impulsive model. The vibrational activity of the products would be associated with the geometrical changes leading the ground parent molecule to the final configuration of the major polyatomic fragments. In the present case, for instance, the geometry of the CH_2BrI in the ground state is pseudotetrahedral—with angles differing from the theoretical 109.5° of the sp^3 hybridization of the carbon atom—while the CH_2X is fairly planar. The departure of the heavy halogen atom imprints a large torque and momentum to the CH_2X moiety which is, in turn, transformed into rotational and vibrational activity, respectively.[21,22]

The soft impulsive model describes quite accurately the contribution b observed in the $Br(^2P_J)$ TEDs shown in Figures 4 and 6, which is safely assigned to a prompt dissociation mechanism along a repulsive surface. Figures 4a and 6a include the vertical bars corresponding to the available energy obtained for the dissociation of CH_2BrI yielding CH_2I products in the $\tilde{X}$ ground state. The reference is located at significantly higher energies than the corresponding dissociation feature. Fast decomposition processes associated with prompt bond-breaking are commonly characterized by narrow translational energy distributions placed at energies slightly above the available energy reference. A large shift between the rise of the distributions and the maximum total available energy indicates that a substantial amount of the energy provided by the photon is communicated as internal energy of the photoproducts. The calculation of the fraction of the available energy channeled into internal DOF of the photofragments, f_{int}, for the prompt dissociation feature, provides values of 0.84 for both $Br(^2P_J)$ fragments, *i.e.*, ~1.2 higher than those obtained at longer wavelengths.[21] In all cases, the dissociation step involves a significant geometrical change of the CH_2I moiety, from distorted pyramidal in the ground and excited states to quasi-planar in the asymptotic dissociative limit (ground state CH_2I ($\tilde{X}$) radicals). The source of the contrast in the energy partitioning at the different dissociation wavelengths must be found in either the excitation step or in the adiabatic passage toward the asymptotic dissociation limit.

As discussed above, absorption at 193 nm takes the parent molecule to the bound $13A'$ state, where dissociation must occur through predissociation of any repulsive state correlating with CH_2I and $Br(^2P_J)$ products. The entanglement of curves which compose the adiabatic picture shown in Figure 7 might complicate the visualization of the decomposition process. It must be considered, however, that certain vibrational activity in the ground CH_2BrI species should most probably assist the absorption. Vibrational excitation in the parent molecule not only enhances the transition probabilities in the Franck–Condon (FC) region but also alters the excited state landscape, bending the symmetry and enabling nonadiabatic transitions between the PECs. Having such prospect in mind, fast decomposition pathways of the excited CH_2BrI can be visualized. Tentatively, the $13A'$ state might proceed successively through two curve crossings via $11A'/11A''$ or $12A'/12A''$, leading to direct dissociation through the $10A'/9A''$ toward the asymptotic CH_2I + Br and CH_2I + Br* limits, respectively. The proposed dissociation picture viewed in light of the soft impulsive model rationalizes the observed experimental features. The excited $13A'$ state is characterized by a CH_2I conformation close to that of the asymptotic limit (*i.e.*, with a Br–C–R angle and C–Br distance substantially different from those of the ground state). At 193 nm excitation, therefore, the geometrical change involved in the process occurs in the excitation step. Once in the excited state, prompt dissociation takes place as discussed above, and the energy accumulated in the distorted CH_2BrI is transferred as momentum (vibration) and torque (rotation) to the internal DOF of the CH_2I moiety.

At 266 nm excitation, CH_2BrI is promoted to the $5A'$ state, while at 210 nm it is excited to the $9A'$ state.[21] A close inspection of Figure 7 (also Figure 8 of ref 21) shows that excitation between 4.66 and 5.90 eV (266–210 nm) leads the parent molecule to a set of curves with a shallow well in the FC region. As such, the excitation step becomes less restricted by geometrical impositions than at 193 nm excitation; in other words, at 266 and 210 nm, the rather wide FC region covers a large range of C–Br distances and CH_2BrI geometries in the excited state. With an accommodated configuration of the excited CH_2BrI, the torque and momentum generated in the departure of the halogen atom would be, consequently, reduced.

The transition from the ground state to the excited $13A'$ state possesses parallel character and, consequently, a value close to the maximum of $\beta = 2$ should be expected for prompt dissociation (within the axial recoil limit). The mechanism described for contribution b involves adiabatic and nonadiabatic

https://doi.org/10.1021/acs.jpca.2c05897
J. Phys. Chem. A 2022, 126, 8404–8422

transitions between different potential energy curves. The geometrical demands of each passing deviate the recoil of the fragments from the axial limit, resulting in a reduced value for the anisotropy parameter.

The $a_0^2(\|)$ polarization parameter takes a value of ∼0.8 for the *b* contribution (see Figure 6). The maximal values indicate that the $Br(^2P_{3/2})$ is exclusively populated in the $m_J = \pm 3/2$ states. Such result turns out to be exceptional if we consider that Br atom's cofragment is a polyatomic radical with high rotational content. The alignment of the $Br(^2P_{3/2})$ atom implies that the projection of the CH_2I rotational angular momentum—or, for all intents and purposes, the rotational angular momentum itself—is greatly constrained along the recoil direction. In light of the soft impulsive model, this constraint implies that the CH_2I fragment does not scramble isotropically; instead, the rotational angular momentum presents a narrow distribution of rotational states, strongly aligned along the recoil direction. The TED associated with a rotational distribution as the one previously described should not cover a broad range of internal energies and would be far from the available energy reference. The *b* component of the Br TED clearly matches those requirements.

The $I(^2P_J)$ + CH_2Br Channels. The TEDs of the $I(^2P_J)$ products present similar qualitative patterns than those of $Br(^2P_J)$, although differ significantly in certain relevant aspects. First of all, the C−I channel is closed at 210 nm excitation and reappears at 193 nm. Second, the TEDs reported at 266 nm show a single contribution—associated with the prompt dissociation mechanism—while at 193 nm the TEDs are qualitatively similar to those obtained for the $Br(^2P_J)$ species. The f_{int} values increase from ∼0.65 at 266 nm to 0.85 at 193 nm for both $I(^2P_J)$ fragments, which supports the idea that the photodecomposition of CH_2BrI into $CH_2Br + I(^2P_J)$ and $CH_2I + Br(^2P_J)$ is ruled by a similar dynamics, and can be rationalized through the soft impulsive model explained in the previous paragraphs.

The vibrational-like structure observed for the prompt bond dissociation featured in the $I^*(^2P_{1/2})$ TED (Figure 6) deserves some further explanation. As discussed for the $Br(^2P_J)$ species, absorption at 193 nm takes the parent molecule to the bound $13A'$ state, where dissociation must occur, in this case, through fast internal conversion to lower excited states and further decomposition onto a repulsive surface (see Figure 8); predissociation through any repulsive state correlating with CH_2Br and $I(^2P_J)$ products seems somehow unreliable since, in contrast to the classical predissociation picture—valid for the $CH_2I + Br(^2P_J)$ channel—where the curve crossing takes place at bond distances close to that of the equilibrium (minima of the PECs), in the current situation the coupling should happen in the steep part of the curves, *i.e.*, far from the FC region. Assuming, therefore, fast internal conversion to a lower state and further dissociation, the vibrational-like structure observed for the $CH_2Br + I^*(^2P_{1/2})$ channel tags the quasi-bound $6A'$ state as the main candidate for the dissociative PEC. The vibrationally assisted diabatic coupling between bound states generates dissociative CH_2Br—I species excited in specific vibrational modes—those mediating in the diabatic coupling—which would unfold in the CH_2Br product. The $CH_2Br + I(^2P_{3/2})$ channel, with no participation of any dissociative-bound state, will show no vibrational structure, emulating the $CH_2I + Br(^2P_J)$ dissociation channels. The proposed dissociation picture explains the observed experimental features, in particular the f_{int} values, in light of the soft impulsive model, in a similar fashion than for the $Br(^2P_J)$ products.

The anisotropy analysis for the $I^*(^2P_{1/2})$ fragment can be drawn in similar terms of those employed for the $Br(^2P_J)$ products. In short, the difference between the experimental anisotropy value, $\beta \simeq 0.8$, and the maximum value of $\beta = 2$ is rationalized in terms of the orientation of the transition dipole moment with respect to the C-I bond as well as of the geometrical changes imposed by the different curve crossings that the molecule undergo in the decomposition pathway. The experimental values for the anisotropy parameter with regard to production of $I(^2P_{3/2})$ atoms show, however, an oscillating increasing tendency along the velocity region of the *b* component, with a maximum value of $\beta \simeq 1$ and a minimum value of $\beta \simeq 0.5$. The variation should be better understood if considered from right to left in the TED. The high energy limit of the distribution, where $\beta \simeq 1$, correlates with CH_2Br fragments with moderate internal energy, *i.e.*, with fragments which had spent less time wandering around the PECs mesh. Since the lost of anisotropy is associated with internal conversion processes, the said fragments will present higher β values. As the kinetic energy is reduced, the available energy transfer into internal DOF of the radical would increase, in parallel to the lost of anisotropy. Remarkably, the oscillations are associated with the vibrational coupling: A vibrational match would generate a fast curve transfer and a subsequent relative small reduction of lost anisotropy.

The $a_0^2(\|)$ polarization parameter takes a value of ∼0 for contribution *b* in the TED of Figure 6. Following the discussion developed for the $Br(^2P_{3/2})$ photofragment, the value reported here indicates no preference of the angular momentum along the recoil direction, a fact that is associated with a broad and unconstrained CH_2Br rotational distribution. The momentum imparted by the I atom during the cleavage is not aligned with respect to any molecular axis, and as a result, the radical product rotates freely around the recoil direction. The corresponding TED shows a rather broad profile (blue and orange lines in Figure 6), in particular, when compared with the same component in the $Br(^2P_{3/2})$ profile.

Branching Ratios, Photofragment Polarization, and Secondary Dissociation. Undoubtedly, the most remarkable differences between the TEDs displayed in Figures 4 and 6 are the branching ratios between the three contributions. The slow-recoil contribution, which is significant for the $Br(^2P_J)$ species becomes particularly intense and strongly dominant for the $I^*(^2P_{1/2})$ and $I(^2P_{3/2})$ products, respectively. The shape of the distribution and the associated anisotropy suggest a multi-photon ionization process, which, in the $I(^2P_J)$ case should be assisted by a resonant excited state, enhancing the absorption of the laser radiation. An additional explanation should be considered, however. Boltzmann distributions in photodissociation processes are usually associated with slow internal conversion of the excited parent molecule to the ground state, where thermal dissociation should occur. The randomization of energy results in distributions characterized by little translational energy. The large branching ratio observed for the $I(^2P_J)$ fragments may be associated, therefore, to a hampered adiabatic dissociation attempt onto an excited PEC. In agreement with a statistical dynamics, the low-recoil contribution shows no particular photofragment polarization, with β and $a_0^2(\|)$ parameters equal to zero.

https://doi.org/10.1021/acs.jpca.2c05897
J. Phys. Chem. A 2022, 126, 8404−8422

The prompt dissociation feature dominates the Br*($^2P_{1/2}$) TEDs and is fairly visible in the I(^2P_J) distributions. In the Br($^2P_{3/2}$) curve, the feature is obscured by the previously undiscussed *c* component. Possible secondary dissociation of the CH_2I and CH_2Br radicals produced after primary C−Br and C−I bond cleavage, respectively, has been considered. Assuming that the polyatomic fragment absorbs a second 193 nm photon from the same pulse (nanosecond time duration), the corresponding energy balance can be written as follows

$$E_{av}^{2^{nd}} = h\nu - D_0(CH_2 - X) - E_{SO}(X) + E_i(CH_2X) - E_i(CH_2) \quad (9)$$

where $E_{av}^{2^{nd}}$ is the available energy in the secondary dissociation process, $D_0(CH_2-X)$ = 2.856 and 3.430 eV are the bond dissociation values for CH_2−I and CH_2−Br, respectively.[54] The term $E_i(CH_2)$ represents the internal energy of the CH_2 coproduct, and $E_i(CH_2X)$ is the internal energy acquired by the polyatomic product on the primary dissociation event. Since the CH_2X fragment is produced with certain distribution of internal energy—represented in Figures 4 and 6 by the *b* contribution—the available energy for the halogen atom produced in the secondary process would vary accordingly.

Table 2. Available Energies, E_{av}, (in eV) for the Possible Primary and Secondary Dissociation Processes[a]

1st dissociation	E_{av}	2nd dissociation	E_{av-max}^{2nd}	E_{av-min}^{2nd}
CH_2I + Br*	3.03	CH_2 + I	6.48	5.51
		CH_2 + I*	5.54	4.57
CH_2Br + I*	3.09	CH_2 + Br	5.90	4.63
		CH_2 + Br*	5.44	4.17
CH_2I + Br	3.49	CH_2 + I	6.47	5.20
		CH_2 + I*	5.53	4.26
CH_2Br + I	4.04	CH_2 + Br	5.93	4.57
		CH_2 + Br*	5.47	4.11

[a] E_{av-max}^{2nd} and E_{av-min}^{2nd} represent the limiting values of the available energy corresponding to $E_i^{max}(CH_2X)$ and $E_i^{min}(CH_2X)$, respectively.

In Table 2, the available energies for the possible dissociation processes are gathered, where $E_{av-max}^{2^{nd}}$ and $E_{av-min}^{2^{nd}}$ represent the limiting values of the available energy corresponding to $E_i^{max}(CH_2X)$ and $E_i^{min}(CH_2X)$, respectively, in the threshold situation in which the CH_2 fragment is produced with no internal energy. The $E_{av}^{2^{nd}}$ references in either case are substantially high-energy shifted with respect of the associated *c* distributions, as expected for secondary processes.

Once the energy requirements have been checked, the Br(^2P_J) and I(^2P_J) images and the corresponding TEDs must be revisited to inspect the consistency of the secondary dissociation assumption. The relative intensity of the Br(^2P_J) and I(^2P_J) images may suggest that dissociation of the C−Br bond is greatly favored at 193 nm excitation with respect to C−I dissociation. The Br($^2P_{3/2}$) TED provides relevant information which might help us to delve into the former statement, in particular when compared to the I($^2P_{3/2}$) distribution. If the images shown in Figures 3 and 5 are analyzed in terms of the predominant feature—setting aside the low-recoil contribution—it should be concluded that (i) the overall intensity of the Br(^2P_J) images is due to both the primary and secondary dissociation processes and (ii) the secondary dissociation of the CH_2I radical is highly unfavored (no secondary dissociation feature is observed in the I*($^2P_{1/2}$) TED). Therefore, it should not be overlooked the fact that although the C−Br bond cleavage is clearly preferred at 193 nm, most of the signal coming from the C−I dissociation is located at the center of the image (stochastic process) and that such signal adds to the secondary source of Br(^2P_J) atoms. Notice that no quantitative branching ratios could be extracted from the present data taking into account the detection method used. Only qualitative comparisons can be done based on the intensity of the images. Further experiments employing other detection methods, such as one-photon VUV ionization, would be necessary to determine the branching ratios between the four atomic fragments.

The stereodynamical data presented in panels b and d of Figures 4 and 6 might illuminate the dynamics behind. Before we proceed, it must be stated that the validity of the photofragment analysis presented in this work is limited to one-photon dissociation processes. Some information for the secondary dissociation process can nevertheless be extracted, although without a proper mathematical treatment, the extension of the analysis is limited. At 193 nm excitation, CH_2BrI can undergo dissociation along both the C−Br and C−I coordinates. Involving two states of the same symmetry, the $13A' \leftarrow \tilde{X}$ transition possesses parallel character, the transition dipole moment $\tilde{\mu}$, however, would form a nonzero angle with either molecular axis. The dissociating bonds, as a consequence, will not be aligned along the polarization direction of the photolysis pulse. With regard to the primary dissociation event (*b* component in the TEDs), the preference for the C−Br bond dissociation suggests that the parent CH_2BrI is preferentially aligned along the C−Br axis in the excitation step at the expenses of the C−I axis, which is in excellent agreement with the different $a_0^2(\|)$ values found for both the Br($^2P_{3/2}$) and I($^2P_{3/2}$) fragments. Furthermore, assuming that the alignment produced by the photolysis pulse is lost due to the rotation during the dissociation step, it must be safely argued that in the steepest part of the PEC, where a second photon might be absorbed, the alignment of the ensemble should be little affected by rotation. If so, a subsequent dissociation of the partially aligned product ensemble would be greatly enhanced if the molecular axis of the dissociating product lies parallel to the polarization of the photolysis laser; and it would be strongly depleted if the said transition is perpendicular to the polarization of the photolysis laser. The relative intensity of the secondary Br(^2P_J) and I(^2P_J) signals fits into the former discussion. CH_2Br−I dissociation is unfavored by geometrical restrictions; the CH_2Br species is produced, nonetheless, with the C−Br bond aligned along the photolysis pulse, and thus, the second absorption and consequent dissociation is highly favored. It could be easily argued that most molecules that dissociate through the C−I bond cleavage should undergo secondary C−Br dissociation. On the other hand, CH_2I−Br dissociation is favored by geometrical restrictions; the CH_2I species would be produced with the C−I axis forming a significant angle with respect to the polarization of the photolysis laser. Secondary dissociation along the C−I bond would be, therefore, clearly hampered.

The former discussion provides a reasonable explanation of the observed branching ratios. To compose a whole picture of the dissociation dynamics, the assumptions made should find agreement with the remaining data provided by the TEDs,

https://doi.org/10.1021/acs.jpca.2c05897
J. Phys. Chem. A 2022, 126, 8404−8422

specifically the photofragment polarization and the energy partitioning. In the $Br(^2P_J)$ TEDs, the anisotropy parameter takes the maximum value of $\beta = 2$ for a parallel transition in the velocity range corresponding to the *c* component. This fact, in conjunction with the large branching ratio obtained for the component at issue, suggests that the CH_2Br radical behaves like a pseudodiatomic, with a well-defined parallel transition dipole moment leading to further dissociation along the C−Br coordinate. In addition, primary dissociation of CH_2BrI into CH_2Br and $I(^2P_J)$ takes place through two different processes, specifically, prompt C−I cleavage (*b* contribution) and slow internal conversion followed by thermal dissociation in the ground state (*a* contribution). In both cases, the CH_2Br fragment is produced with substantial internal (rotational and vibrational) excitation, although with different partitioning (the *b* profile reproduces specific rotational and vibrational excitation, while the *a* contribution is characterized by randomized distribution of the rovibrational excitation). Accordingly, a broad and unstructured translational distribution, located at substantial distance from the corresponding available energy reference (indicating the formation of CH_2 fragments with high internal energy), should be expected for the secondary dissociation of CH_2Br. The prediction reflects quite accurately the profiles obtained for the *c* component in panel b of Figures 4 and 6.

Likewise, a similar discussion may be developed for the $I(^2P_J)$ species. The *c* component in the corresponding TEDs might be considered almost negligible for both $I(^2P_J)$ products. In addition, the associated β parameter takes values close to zero. The reduced values of β suggest, as in the case of CH_2Br, that the CH_2I radical behaves like a pseudodiatomic, with a well-defined parallel transition dipole moment leading to further dissociation along the C−I coordinate; in this case, however, the absorption of a second photon would be highly hampered by the disadvantageous orientation of the C−I axis with respect to the polarization of the photolysis laser. The energy partitioning of the minor *c* component for the $I(^2P_J)$ species is explained in similar terms than that made for $Br(^2P_J)$. In short, the CH_2I fragments would be produced with significant internal energy, leading to broad TEDs associated with the formation of CH_2 fragments with high content of internal energy.

CONCLUSIONS

The main conclusions of the present work are summarized as follows: The translational energy distributions for the $Br(^2P_J)$ and $I(^2P_J)$ (with $J = 3/2$ and $1/2$ for Br/I and Br*/I*, respectively) atomic photofragments are interpreted in terms of three contributions, associated to prompt C−X dissociation, a stochastic process and a secondary CH_2X dissociation process. At 193 nm excitation, those CH_2BrI molecules whose C−Br molecular axis is aligned parallel to the electric field of the photolysis pulse are preferentially excited. As a result, cleavage of the C−Br bond is greatly favored with respect to C−I dissociation for both CH_2XY and CH_2X (where X and Y are either halogen atom, Br or I) species. Prompt C−Br dissociation takes place after excitation at the $13A'$ electronic state and predissociation through the $11A'/11A''$ or $12A'/12A''$ states, leading to direct dissociation through the $10A'/9A''$ states for the CH_2I + Br and CH_2I + Br*, respectively.

Bond C−I dissociation takes place after excitation at the $13A'$ state but is not assisted by predissociation. Instead, fast internal conversion to lower electronic states and subsequent dissociation through the $6A'/6A''$ and $4A'/4A''$ results in relative fast $I(^2P_J)$ fragments and in a predominant low-recoil Boltzmann-like contribution associated to the partially frustrated prompt C−I bond cleavage.

The prompt bond dissociation dynamics is well interpreted in terms of the soft impulsive model which predicts a large fraction of the available energy transferred into rotation of the polyatomic CH_2X fragment. The CH_2X products show as well a considerable amount of vibrational energy due to the geometrical changes produced in the curve crossings leading to the dissociation limits. In the case of the first dissociation event (*b* contribution), the photofragment polarization analysis performed in terms of the $a_q^k(p)$ parameters suggest that the rotational angular momentum of the CH_2I species is produced with a high degree of alignment around the recoil direction.

ASSOCIATED CONTENT

Supporting Information

The Supporting Information is available free of charge at https://pubs.acs.org/doi/10.1021/acs.jpca.2c05897.

High-resolution UV−VUV gas phase CH_2BrI absorption spectrum and assignments. (PDF)

AUTHOR INFORMATION

Corresponding Author

Luis Bañares − *Departamento de Química Física (Unidad Asociada I+D+i al CSIC), Facultad de Ciencias Químicas, Universidad Complutense de Madrid, 28040 Madrid, Spain; Instituto Madrileño de Estudios Avanzados en Nanociencia (IMDEA-Nanoscience), 28049 Madrid, Spain;* orcid.org/0000-0002-0777-2375; Email: lbanares@ucm.es

Authors

Pedro Recio − *Departamento de Química Física (Unidad Asociada I+D+i al CSIC), Facultad de Ciencias Químicas, Universidad Complutense de Madrid, 28040 Madrid, Spain;* orcid.org/0000-0002-4867-2872

Javier Cachón − *Departamento de Química Física (Unidad Asociada I+D+i al CSIC), Facultad de Ciencias Químicas, Universidad Complutense de Madrid, 28040 Madrid, Spain*

Luis Rubio-Lago − *Departamento de Química Física (Unidad Asociada I+D+i al CSIC), Facultad de Ciencias Químicas, Universidad Complutense de Madrid, 28040 Madrid, Spain*

David V. Chicharro − *Departamento de Química Física (Unidad Asociada I+D+i al CSIC), Facultad de Ciencias Químicas, Universidad Complutense de Madrid, 28040 Madrid, Spain; Quantum Dynamics & Control, Max Planck Institute for Nuclear Physics (MPIK), 69117 Heidelberg, Germany*

Alexandre Zanchet − *Instituto de Física Fundamental, Consejo Superior de Investigaciones Científicas, 28006 Madrid, Spain*

Paulo Limão-Vieira − *Atomic and Molecular Collisions Laboratory, CEFITEC, Department of Physics, Universidade NOVA de Lisboa, 2829-516 Caparica, Portugal;* orcid.org/0000-0003-2696-1152

Nelson de Oliveira − *Synchrotron SOLEIL, L'Orme des Merisiers, 91192 Gif sur Yvette, France*

Peter C. Samartzis − *Institute of Electronic Structure and Laser, Foundation for Research and Technology-Hellas (FORTH-IESL), 70013 Heraklion, Greece;* orcid.org/0000-0001-8873-2326

Sonia Marggi Poullain − *Departamento de Química Física (Unidad Asociada I+D+i al CSIC), Facultad de Ciencias*

https://doi.org/10.1021/acs.jpca.2c05897
J. Phys. Chem. A 2022, 126, 8404−8422

Químicas, Universidad Complutense de Madrid, 28040 Madrid, Spain; orcid.org/0000-0001-6712-3628

Complete contact information is available at: https://pubs.acs.org/10.1021/acs.jpca.2c05897

Notes

The authors declare no competing financial interest.

■ ACKNOWLEDGMENTS

P.R. is grateful to Universidad Complutense de Madrid (UCM) for a Margarita Salas postdoctoral contract. J.C. and D.V.C. acknowledge financial support from Spanish Ministry of Science and Innovation under the FPI predoctoral program. P.L.-V. acknowledges Fundación Carolina for a mobility grant at UCM under the Programa de Movilidad de Profesores e Investigadores Portugueses (Fundación Endesa). Part of the experiments presented were performed at the DESIRS beamline at synchrotron SOLEIL under proposal number 20170473. We acknowledge SOLEIL for provision of synchrotron radiation facilities. This work was performed in part at the Institute of Electronic Structure and Laser, Foundation for Research and Technology-Hellas (IESL-FORTH) and received financial support from LaserLab Europe (Grant agreement No. 654148) through the ULF-FORTH002540 project. This research has been carried out within the Unidad Asociada Química Física Molecular between the Departamento de Química Física of Universidad Complutense de Madrid and CSIC. This project has received funding from the Spanish Ministry of Science and Innovation (Grants PGC2018-096444-B-I00 and PID2019-107115GB-C21).

■ ADDITIONAL NOTES

[a]The Br*($^2P_{1/2}$) or I*($^2P_{1/2}$) photofragments possess a total angular momentum J = 1/2 and cannot show angular polarization (alignment or orientation).

[b]The relationship between $A_q^k(p)$ coefficients and the $a_q^k(p)$ parameters can be found in eqs ^{4}a−^{4}d of ref 34.

■ REFERENCES

(1) Saiz-Lopez, A.; Plane, J. M. C.; Baker, A. R.; Carpenter, L. J.; von Glasow, R.; Gómez Martín, J. C.; McFiggans, G.; Saunders, R. W. Atmospheric Chemistry of Iodine. *Chem. Rev.* **2012**, *112*, 1773−1804.

(2) Simpson, W. R.; Brown, S. S.; Saiz-Lopez, A.; Thornton, J. A.; von Glasow, R. Tropospheric Halogen Chemistry: Sources, Cycling, and Impacts. *Chem. Rev.* **2015**, *115*, 4035−4062.

(3) Welz, O.; Savee, J. D.; Osborn, D. L.; Vasu, S. S.; Percival, C. J.; Shallcross, D. E.; Taatjes, C. A. Direct Kinetic Measurements of Criegee Intermediate (CH_2OO) Formed by Reaction of CH_2I with O_2. *Science* **2012**, *335*, 204−207.

(4) Eskola, A. J.; Wojcik-Pastuszka, D.; Ratajczak, E.; Timonen, R. S. Kinetics of the reactions of CH_2Br and CH_2I radicals with molecular oxygen at atmospheric temperatures. *Phys. Chem. Chem. Phys.* **2006**, *8*, 1416−1424.

(5) Jones, C. E.; Carpenter, L. J. Solar Photolysis of CH_2I_2, CH_2ICl, and CH_2IBr in Water, Saltwater, and Seawater. *Environ. Sci. Technol.* **2006**, *40*, 1372.

(6) Mossinger, J. C.; Shallcross, D. E.; Anthony Cox, R. UV−VIS Absorption Cross-Sections and Atmospheric Lifetimes of CH_2Br_2,CH_2I_2 and CH_2BrI. *J. Chem. Soc., Faraday Trans.* **1998**, *94*, 1391−1396.

(7) Man, S.; Kwok, W. M.; Phillips, D. L.; Johnson, A. E. Short-time photodissociation dynamics of A-band and B-band bromoiodomethane in solution: An examination of bond selective electronic excitation. *J. Chem. Phys.* **1996**, *105*, 5842.

(8) Butler, L. J.; Hintsa, E. J.; Shane, S. F.; Lee, Y. T. The electronic state-selective photodissociation of CH_2BrI at 248, 210, and 193 nm. *J. Chem. Phys.* **1987**, *86*, 2051.

(9) Lee, S. J.; Bersohn, R. Photodissociation of a molecule with two chromophores. CH_2IBr. *J. Phys. Chem.* **1982**, *86*, 728−730.

(10) Liu, K.; Zhao, H.; Wang, C.; Zhang, A.; Ma, S.; Li, Z. A theoretical study of bond selective photochemistry in CH_2BrI. *J. Chem. Phys.* **2005**, *122*, 044310.

(11) Liu, Y.-J.; Ajitha, D.; Krogh, J. W.; Tarnovsky, A. N.; Lindh, R. Spin−Orbit Ab Initio Investigation of the Photolysis of Bromoiodomethane. *ChemPhysChem* **2006**, *7*, 955−963.

(12) Tang, K.-C.; Peng, J.; Spears, K. G.; Sension, R. J. Photoinitiated bond dissociation of bromoiodomethane in solution: Comparison of one-photon and two-photon excitations and the formation of iso-CH_2Br−I and iso-CH_2I−Br. *J. Chem. Phys.* **2010**, *132*, 141102.

(13) Anderson, C. P.; Spears, K. G.; Wilson, K. R.; Sension, R. J. Solvent dependent branching between C-I and C-Br bond cleavage following 266 nm excitation of CH_2BrI. *J. Chem. Phys.* **2013**, *139*, 194307.

(14) Attar, A. R.; Piticco, L.; Leone, S. R. Core-to-valence spectroscopic detection of the CH_2Br radical and element-specific femtosecond photodissociation dynamics of CH_2BrI. *J. Chem. Phys.* **2014**, *141*, 164308.

(15) Horton, S. L.; Liu, Y.; Forbes, R.; Makhija, V.; Lausten, R.; Stolow, A.; Hockett, P.; Marquetand, P.; Rozgonyi, T.; Weinacht, T. Excited state dynamics of CH_2I_2 and CH_2BrI studied with UV pump VUV probe photoelectron spectroscopy. *J. Chem. Phys.* **2019**, *150*, 174201.

(16) Liu, Y.; Rozgonyi, T.; Marquetand, P.; Weinacht, T. Excited-state dynamics of CH_2I_2 and CH_2IBr studied with UV-pump VUV-probe momentum-resolved photoion spectroscopy. *J. Chem. Phys.* **2020**, *153*, 184304.

(17) Burt, M.; et al. Coulomb-explosion imaging of concurrent CH_2BrI photodissociation dynamics. *Phys. Rev. A* **2017**, *96*, 043415.

(18) Köckert, H.; et al. UV-induced dissociation of CH_2BrI probed by intense femtosecond XUV pulses. *J. Phys. B: At. Mol. Opt. Phys.* **2022**, *55*, 014001.

(19) Pan, C.; Zhang, Y.; Lee, J. D.; Kidwell, N. M. Imaging the dynamics of CH_2BrI photodissociation in the near ultraviolet region. *J. Phys. Chem. A* **2018**, *122*, 3728−3734.

(20) Muthiah, B.; Paredes-Roibás, D.; Kasai, T.; Lin, K.-C. Photodissociation of CH_2BrI using cavity ring-down spectroscopy: in search of a BrI elimination channel. *Phys. Chem. Chem. Phys.* **2019**, *21*, 13943.

(21) Marggi Poullain, S.; Chicharro, D. V.; Navarro, E.; Rubio-Lago, L.; González-Vázquez, J.; Bañares, L. Photodissociation dynamics of bromoiodomethane from the first and second absorption bands. A combined velocity map and slice imaging study. *Phys. Chem. Chem. Phys.* **2018**, *20*, 3490.

(22) Murillo-Sánchez, M. L.; Marggi Poullain, S.; Bajo, J. J.; Corrales, M. E.; González-Vázquez, J.; Solá, I. R.; Bañares, L. Halogen-atom effect on the ultrafast photodissociation dynamics of the dihalomethanes CH_2ICl and CH_2BrI. *Phys. Chem. Chem. Phys.* **2018**, *20*, 20766.

(23) de Oliveira, N.; Roudjane, M.; Joyeux, D.; Phalippou, D.; Rodier, J.-C.; Nahon, L. High-resolution broad-bandwidth Fourier-transform absorption spectroscopy in the VUV range down to 40 nm. *Nat. Photonics* **2011**, *5*, 149−153.

(24) Nahon, L.; de Oliveira, N.; Garcia, G. A.; Gil, J.-F.; Joyeux, D.; Lagarde, B.; Polack, F. DESIRS: a state-of-the-art VUV beamline featuring high resolution and variable polarization for spectroscopy and dichroism at SOLEIL. *J. Phys.: Conf. Ser.* **2013**, *425*, 122004.

(25) de Oliveira, N.; Joyeux, D.; Roudjane, M.; Gil, J.-F.; Pilette, B.; Archer, L.; Ito, K.; Nahon, L. The high-resolution absorption spectroscopy branch on the VUV beamline DESIRS at SOLEIL. *J. Synchrotron Rad.* **2016**, *23*, 887−900.

(26) de Oliveira, N.; Joyeux, D.; Phalippou, D.; Rodier, J. C.; Polack, F.; Vervloet, M.; Nahon, L. A Fourier transform spectrometer without a beam splitter for the vacuum ultraviolet range: From the optical design to the first UV spectrum. *Rev. Sci. Instrum.* **2009**, *80*, 043101.

(27) Gebhardt, C. R.; Rakitzis, T. P.; Samartzis, P. C.; Ladopoulos, V.; Kitsopoulos, T. N. Slice imaging: A new approach to ion imaging and velocity mapping. *Rev. Sci. Instrum.* **2001**, *72*, 3848−3853.
(28) Papadakis, V.; Kitsopoulos, T. N. Slice imaging and velocity mapping using a single field. *Rev. Sci. Instrum.* **2006**, *77*, 083101.
(29) Rodríguez, J. D.; González, M. G.; Rubio-Lago, L.; Bañares, L.; Samartzis, P. C.; Kitsopoulos, T. N. Stereodynamics of the Photodissociation of Nitromethane at 193 nm: Unravelling the Dissociation Mechanism. *J. Phys. Chem. A* **2013**, *117*, 8175−8183.
(30) Marggi Poullain, S.; González, M. G.; Samartzis, P. C.; Kitsopoulos, T. N.; Rubio-Lago, L.; Bañares, L. New insights into the photodissociation of methyl iodide at 193 nm: stereodynamics and product branching ratios. *Phys. Chem. Chem. Phys.* **2015**, *17*, 29958−29968.
(31) Kim, Y. S.; Jung, Y.-J.; Kang, W.; Jung, K.-H. Photoelectron imaging spectroscopy for (2 + 1) resonance-enhanced multiphoton ionization of atomic bromine. *Bull. Korean Chem. Soc.* **2002**, *23*, 189.
(32) Jung, Y.-J.; Shin Kim, Y.; Kyung Kang, W.; Jung, K.-H. Photoelectron imaging spectroscopy for (2 + 1) resonance-enhanced multiphoton ionization of atomic iodine produced from A-band photolysis of CH3I. *J. Chem. Phys.* **1997**, *107*, 7187.
(33) Rakitzis, T. P.; Zare, R. N. Photofragment angular momentum distributions in the molecular frame: Determination and interpretation. *J. Chem. Phys.* **1999**, *110*, 3341.
(34) Rakitzis, T. P. Direct measurements of photofragment alignment from unnormalized Abel-inverted images. *Chem. Phys. Lett.* **2001**, *342*, 121−126.
(35) Rakitzis, T. P.; Samartzis, P. C.; Kitsopoulos, T. N. Complete Measurement of $S(^1D_2)$ Photofragment Alignment from Abel-Invertible Ion Images. *Phys. Rev. Lett.* **2001**, *87*, 123001.
(36) Rakitzis, T. P.; Kitsopoulos, T. N. Measurement of Cl and Br photofragment alignment using slice imaging. *J. Chem. Phys.* **2002**, *116*, 9228.
(37) Rakitzis, T.; Samartzis, P.; Toomes, R.; Tsigaridas, L.; Coriou, M.; Chestakov, D.; Eppink, A.; Parker, D.; Kitsopoulos, T. Photofragment alignment from the photodissociation of HCl and HBr. *Chem. Phys. Lett.* **2002**, *364*, 115−120.
(38) Orr-Ewing, A.; Zare, R. N. Orientation and Alignment of Reaction Products. *Annu. Rev. Phys. Chem.* **1994**, *45*, 315−366.
(39) Samartzis, P. C.; Bakker, B. L. G.; Rakitzis, T. P.; Parker, D. H.; Kitsopoulos, T. N. Spin-orbit branching ratios for the Cl atom photofragments following the excitation of Cl_2 from 310 to 470 nm. *J. Chem. Phys.* **1999**, *110*, 5201.
(40) Werner, H.-J.et al.*MOLPRO, A Package of Ab Initio Programs*, ver. 2015.1; 2015.
(41) Werner, H.-J. Third-order multireference perturbation theory The CASPT3 method. *Mol. Phys.* **1996**, *89*, 645.
(42) Werner, H.-J.; Knowles, P. J. A second order multiconfiguration SCF procedure with optimum convergence. *J. Chem. Phys.* **1985**, *82*, 5053.
(43) Berning, A.; Schweizer, M.; Werner, H.-J.; Knowles, P. J.; Palmieri, P. Spin-orbit matrix elements for internally contracted multireference configuration interaction wavefunctions. *Mol. Phys.* **2000**, *98*, 1823.
(44) Lee, M.; Kim, H.; Lee, Y. S.; Kim, M. S. One-photon mass-analyzed threshold ionization spectroscopy of CH_2BrI: Extensive bending progression, reduced steric effect, and spin-orbit effect in the cation. *J. Chem. Phys.* **2005**, *123*, 024310.
(45) Penner, A.; Amirav, A. Rydberg state absorption spectroscopy of $Br(CH_2)_nI$ (n = 1−3). *J. Chem. Phys.* **1990**, *93*, 8576−8579.
(46) Man, S.-Q.; Kwok, W. M.; Phillips, D. L. Investigation of bond-selective electronic excitation in bromoiodomethane. *J. Phys. Chem.* **1995**, *99*, 15705−15708.
(47) Liu, Y.-J.; Ajitha, D.; Krogh, J. W.; Tarnovsky, A. N.; Lindh, R. Spin−Orbit Ab Initio Investigation of the Photolysis of Bromoiodomethane. *ChemPhysChem: A European Journal of Chemical Physics and Physical Chemistry* **2006**, *7*, 955−963.
(48) Zheng, X.; Phillips, D. L. Photoisomerization reaction of CH_2BrI following *A*-band and *B*-band photoexcitation in the solution phase: Transient resonance Raman observation of the iso-CH_2I−Br photoproduct. *J. Chem. Phys.* **2000**, *113*, 3194−3203.
(49) Sándor, P.; Zhao, A.; Rozgonyi, T.; Weinacht, T. Strong field molecular ionization to multiple ionic states: direct versus indirect pathways. *Journal of Physics B: Atomic, Molecular and Optical Physics* **2014**, *47*, 124021.
(50) Muckerman, J. T. J. Information Theoretic Prior Functions for Large Molecular Systems. *J. Phys. Chem.* **1989**, *93*, 179−184.
(51) Irikura, K. K.; Johnson, R. D.; Hudgens, J. W. Two new electronic states of CH_2. *J. Phys. Chem.* **1992**, *96*, 6131.
(52) Busch, G. E.; Wilson, K. R. Triatomic Photofragment Spectra. I. Energy Partitioning in NO_2 Photodissociation. *J. Chem. Phys.* **1972**, *56*, 3626−3638.
(53) Brynteson, M. D.; Womack, C. C.; Booth, R. S.; Lee, S.-H.; Lin, J. J.; Butler, L. J. Radical intermediates in the addition of OH to propene: photolytic precursors and angular momentum effects. *J. Phys. Chem. A* **2014**, *118*, 3211−3229.
(54) Lazarou, Y. G.; Prosmitis, A. V.; Papadimitriou, V. C.; Papagiannakopoulos, P. Theoretical calculation of bond dissociation energies and enthalpies of formation for halogenated molecules. *J. Phys. Chem. A* **2001**, *105*, 6729.

https://doi.org/10.1021/acs.jpca.2c05897
J. Phys. Chem. A 2022, 126, 8404−8422